Convection and Easterly Wave Structures Observed in the Eastern Pacific Warm Pool during EPIC-2001

WALTER A. PETERSEN

NSSTC/ESSC, University of Alabama in Huntsville, Huntsville, Alabama

ROBERT CIFELLI

Department of Atmospheric Science, Colorado State University, Fort Collins, Colorado

DENNIS J. BOCCIPPIO

NASA Marshall Space Flight Center, Huntsville, Alabama

STEVEN A. RUTLEDGE

Department of Atmospheric Science, Colorado State University, Fort Collins, Colorado

CHRIS FAIRALL

NOAA/ETL, Boulder, Colorado

ABSTRACT

During September–October 2001, the East Pacific Investigation of Climate Processes in the Coupled Ocean–Atmosphere System (EPIC-2001) intertropical convergence zone (ITCZ) field campaign focused on studies of deep convection in the warm-pool region of the eastern Pacific. This study combines C-band Doppler radar, sounding, and surface heat flux data collected aboard the R/V *Ronald H. Brown* during EPIC to describe the kinematic and thermodynamic states of the ITCZ environment, together with tendencies in convective structure, lightning, rainfall, and surface heat fluxes as a function of 3–5-day easterly wave phase.

Three easterly waves were observed at the location of the R/V *Brown* during EPIC-2001. Wind and thermodynamic data reveal that the wave trough axes exhibited positively correlated u and v winds, a slight westward phase tilt with height, and relatively strong (weak) northeasterly tropospheric shear following the trough (ridge) axis. Temperature and humidity perturbations exhibited mid- to upper-level cooling (warming) and drying (moistening) in the northerly (trough and southerly) phase. At low levels, warming (cooling) and moistening (drying) occurred in the northerly (southerly) phase.

Composited radar, sounding, lightning, and surface heat flux observations suggest the following systematic behavior as a function of wave phase: zero to one-quarter wavelength ahead of (behind) the wave trough in northerly (southerly) flow, larger (smaller) convective available potential energy (CAPE), lower (higher) convective inhibition (CIN), weaker (stronger) tropospheric shear, larger (smaller) convective rain fractions, higher (lower) conditional mean rain rates, higher (lower) lightning flash densities, and more (less) robust convective vertical structure occurred. Latent and sensible heat fluxes reached a minimum in the northerly phase and then increased through the trough, reaching a peak during the ridge phase (leading the peak in CAPE). Larger areas of light convective and stratiform rain and slightly larger (10%) area-averaged rain rates occurred in the vicinity of, and just behind, the trough axes in southerly and ridge flow. Importantly, the transition in convective structure observed across the trough axis when considered with the relatively small change in area mean rain rates suggests the presence of a transition in the vertical structure of diabatic heating across the easterly waves examined. The inferred transition in heating structure is supported by radar-diagnosed divergence profiles that exhibit convective (stratiform) characteristics ahead of (behind) the trough.

1. Introduction

Westward-moving disturbances with periods of 2–7 days are a dominant mode of synoptic variability in the Tropics. These include classic tropical 3–5-day "easterly wave" or "tropical depression" disturbances (e.g., Riehl 1954; Yanai et al. 1968; Burpee 1972, 1974, 1975; Lau and Lau 1990), and/or longer wavelength near-equatorial mixed Rossby–gravity wave modes (MRGs; e.g., Liebman and Hendon 1990). Both easterly waves and MRGs migrate across various continents and ocean

Corresponding author address: Dr. Walter A. Petersen, NSSTC/ESSC, University of Alabama in Huntsville, Huntsville, AL 35899. E-mail: walt.petersen@msfc.nasa.gov

basins (e.g., Lau and Lau 1990; Avila and Pasch 1992; Serra and Houze 2002) providing a high-frequency modulation of climatological convection situated along the intertropical convergence zone (ITCZ; e.g., Gu and Zhang 2002). Importantly, easterly waves often provide the requisite forcing for tropical cyclogenesis (e.g., Avila and Pasch 1992; Landsea et al. 1998; Thorncroft and Hodges 2001). Consequently, a plethora of observational and modeling studies have examined the kinematic, thermodynamic, and precipitation characteristics associated with these waves over several different regions of the globe, including the equatorial Atlantic Ocean and Africa [e.g., African easterly waves (AEWs); Burpee 1972, 1974; Holton 1971; Reed et al. 1977; Nitta 1977; Thompson et al. 1979; Stevens 1979; Reed et al. 1988; Duvel 1990; Jenkins and Cho 1991; Grabowski et al. 1996; Donner et al. 1999; Xu and Randall 2001], the Caribbean (Riehl 1954; Yanai and Nitta 1967; Shapiro 1986), the eastern Pacific Ocean (Molinari et al. 1997; Raymond et al. 1998; Zehnder et al. 1999; Molinari et al. 2000; Serra and Houze 2002), and the western Pacific Ocean (Yanaii and Nitta 1967; Chang et al. 1970; Reed and Recker 1971).

For the most part the aforementioned studies have relied on limited sounding, satellite, and model analyses to describe the three-dimensional (3D) kinematic structure of tropical easterly waves. Outgoing longwave radiation (OLR) and/or limited radar studies (land, sea, and airborne) have been used in a complimentary fashion to describe the spatial and temporal coverage of precipitation, convection, and air flow in relation to wave phase in the horizontal plane (e.g., Hudlow 1979; Thompson et al. 1979; Raymond et al. 1998; Serra and Houze 2002). However, detailed continuous observations of the symbiotic relationship between convective *vertical structure* and easterly wave phase are few in number. This is an important point from a physical perspective because 1) convective structure and the vertical profile of diabatic heating are closely related, 2) the diabatic heating structure provides a strong feedback to the development and maintenance of the wave circulation (e.g., Norquist et al. 1977; Albignat and Reed 1980; Kwon and Mak 1990; Thorncroft and Hodges 2001), and 3) cumulus transports of momentum may also affect wave dynamics (e.g., Stevens 1979; Shapiro 1986).

From a numerical modeling perspective, the ubiquitous nature of easterly waves and their influence on tropical weather and climate require an accurate representation of this mode of synoptic variability in operational forecast and climate models. To the extent that cloud-resolving model (CRM) simulations are utilized in the development of subgrid-scale convective parameterizations for large-scale numerical models (Grabowski et al. 1996; Donner et al. 1999; Xu and Randall 2001), it is clear that observational validation of CRM 3D convective structure as it relates to the temporal evolution of wave phase is important.

For example, the CRM studies of Donner et al. (1999) and Xu and Randall (2001) both identify transitions in convective regime (also manifested in vertical structure) that occur as simulated AEWs transition from pre- to posttrough phase. Both modeling studies simulated deeper and more intense convection in the pretrough phase, followed by a mixture of deep convection and stratiform clouds in the trough phase, and a more stratiform structure in the posttrough phase. Simulated transitions in convective structure occurred in the presence of relatively large rainfall rates implying an accompanying evolution in the vertical structure of diabatic heating. The observational studies cited above, while providing useful information for validating the aforementioned CRM-simulated area mean rainfall rates and cloud coverage, etc., provide little in the way of validation of CRM convective structure and/or cloud microphysics (including critical microphysical processes) as a function of easterly wave phase in the vertical.

In this study we provide detailed four-dimensional (4D) sounding and C-band radar observations of the precipitation structure in convection as it relates to the kinematic and thermodynamic properties of easterly waves observed in the warm pool of the eastern Pacific Ocean (10°N, 95°W). These observations were collected during the Eastern Pacific Investigation of Climate Processes in the Coupled Ocean–Atmosphere System 2001 (EPIC-2001), intertropical convergence zone field campaign (Cronin et al. 2002; Raymond et al. 2003, hereafter R03).

2. The EPIC-2001 ITCZ field campaign

The EPIC-2001 intensive field campaign took place during the months of September and October 2001. The field campaign consisted of two phases: 1) studies of deep convection in the warm-pool region of the eastern Pacific ITCZ cold tongue complex centered near 10°N, 95°W (Fig. 1) from early September to early October 2001 (R03); and 2) studies of stratocumulus cloud microphysics off the west coast of South America (early to late October 2001). Herein, we focus on the EPIC ITCZ field phase (Fig. 1).

The overarching objective for the atmospheric component of the EPIC ITCZ field campaign was to determine what physical processes control the location, strength, and other characteristics of eastern Pacific ITCZ convection. More specifically, what mechanism(s) are responsible for the location and forcing of convection in the eastern Pacific ITCZ over timescales ranging from the diurnal to intraseasonal?

Platforms and instrumentation

In order to address experiment objectives, several ship-based and airborne observational platforms were deployed during the field phase. These platforms included the National Oceanic and Atmospheric Admin-
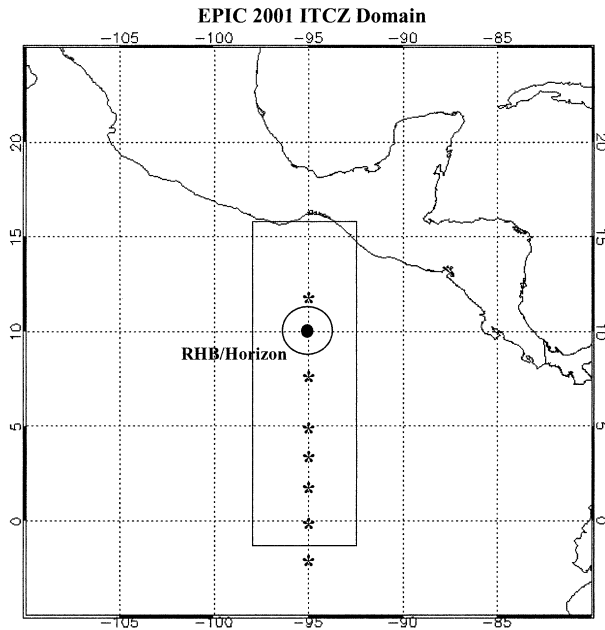
EPIC 2001 ITCZ Domain

FIG. 1. Map of EPIC-2001 ITCZ operating area. The nominal positions of the *RHB* and R/V *Horizon* are indicated by a black circle. A 150-km range ring centered on the location of the *RHB* radar is also indicated. Buoy locations in the eastern portion of the enhanced TAO mooring array are indicated by (*), and the general aircraft operating area is indicated by a rectangle. Note that there is also a TAO mooring located at 10°N, 95°W.

istration (NOAA) and National Science Foundation (NSF) research vessels, R/V *Ronald H. Brown* (*RHB*) and R/V *Horizon,* respectively, and NOAA P-3 and NSF/National Center for Atmospheric Research (NCAR) C-130 aircraft. The *RHB* and R/V *Horizon* operated continuously for approximately 21 days (12 September–1 October) about a fixed point in the ITCZ located at 10°N, 95°W along the eastern edge of the Tropical Atmosphere–Ocean (TAO) mooring array (enhanced by adding buoys at 3.5°, 10°, and 12°N along the 95°W meridian; Cronin et al. 2002).

In addition to conducting a host of oceanographic measurements (Cronin et al. 2002), the *RHB* carried a variety of atmospheric instrumentation including an inertially stabilized C-band Doppler radar (Ryan et al. 2002) for precipitation and convective structure measurements (Table 1). The inertial stabilization of the radar enables antenna-pointing accuracy to be maintained even in disturbed seas, resulting in mean antenna-pointing errors during the ITCZ cruise of less than 0.2°–0.4° (via daily solar calibrations; R. Bowie 2001, personal communication). The *RHB* also carried a Ka-band Doppler cloud radar (nonstabilized), NOAA/Environmental Technology Laboratory mini-MOPA lidar, 915-MHz wind profiler, Vaisala GPS sounding system, NOAA/ETL surface radiative and turbulent latent and sensible heat flux system, automated surface meteorological instruments, aerosol sampling equipment, a ceil-

TABLE 1. EPIC ITCZ *RHB* C-band radar operating parameters.

Wavelength	5.4 cm (5.595 GHz)
Transmit power	250 kW
Beamwidth	0.95°
Antenna rotation rate	18° s^{-1}
Pulse repetition frequency: surveillance scans/ volume scans	500/910 Hz
Pulse width: surveillance scans/volume scans	2/1.2 μs
Gate spacing	250 m

ometer, and a suite of rain gauges (e.g., Yuter and Houze 2000).

As a compliment to the *RHB* measurements, the R/V *Horizon* carried a Joss–Waldvogel disdrometer for raindrop size distribution measurements, an S-band wind profiler (used as a vertically pointing Doppler radar), and a suite of rain gauges. During field operations the *RHB* moved continuously within a 10-km radius circle centered on the TAO mooring located at 10°N, 95°W, while the R/V *Horizon* executed "butterfly" patterns within a 60–80-km radius of the *RHB* and TAO mooring collecting oceanographic mixed-layer measurements and atmospheric precipitation measurements under the coverage umbrella of the *RHB* C-band radar.

In order to produce surface precipitation maps and a high-resolution unbiased time series of 3D convective structure, the *RHB* C-band radar was operated 24 h day^{-1} in a 10-min cycle of 360° surveillance scans, 360° volume scans, and range–height indicator (RHI) scans (Table 2). Volume scan data were collected in either distant, near, or extended velocity azimuth display (EVAD; useful for computing divergence and vertical motion) modes depending on the depth and coverage of convection around the ship (Table 2). Radar-diagnosed rainfall, 3D convective structure, and divergence were then analyzed within the context of a host of atmospheric variability timescales (diurnal through intraseasonal) by utilizing atmospheric sounding data collected from the RHB at a frequency of 6 times per day nominally near the hours of 0300, 0700, 1100, 1500, 1900, 00, and 2300 UTC.

With regard to the radar and sounding analysis in this study, we take a statistical approach analogous to that

TABLE 2. EPIC ITCZ *RHB* C-band radar scan elevation angles.

Scan	Elevation angles (°)
Surveillance/rain	0.5, 1.3, 2.1
Far	0.5, 1.3, 2.1, 2.9, 3.6, 4.5, 5.4, 6.4, 7.4, 8.5, 9.8, 11.2, 12.8, 14.8, 16.8, 19.2, 22.2, 26.0, 30.0, 35.0
Near	0.5, 1.3, 2.1, 3.0, 4.2, 5.7, 7.4, 9.0, 11.0, 15.0, 18.0, 22.0, 26.0, 30.0, 34.0, 39.0, 44.0, 50.0, 55.0, 60.0
EVAD	0.8, 1.5, 3.2, 5.5, 7.9, 10.3, 12.7, 15.1, 17.6, 20.0, 22.6, 25.1, 27.8, 30.5, 33.2, 36.1, 39.1, 42.2, 45.4, 48.9, 53.4

of DeMott and Rutledge (1998a,b) who utilized ship-based C-band radar observations with sounding data to examine ensemble convective structure and rainfall variability as a function of 30–60-day variability over the western Pacific. More specifically, we focus on easterly wave variability with timescales on the order of 2–7 days, utilizing the *RHB* C-band Doppler radar, sounding, and surface heat flux observations to provide a comprehensive description of the 4D structure of ITCZ convection as a function of wave phase.

3. Data and analysis methodology

a. RHB sounding data

The sounding data files used in this study were quality controlled (QC) after the EPIC-2001 field campaign by the University Corporation for Atmospheric Research (UCAR) Joint Office for Scientific Support (JOSS) using algorithms summarized in Loehrer et al. (1996). As a final QC measure we (a) removed all thermodynamic and wind field data flagged as "bad" in the JOSS data files, and (b) also eliminated data levels possessing spuriously large temperature lapse rates (with the exception of good wind data) using the rather conservative constraint that atmospheric lapse rates below the tropopause and above the surface layer could not exceed $\pm 20°C$ km^{-1}. The eliminated thermodynamic data, and if necessary vector wind components, were subsequently replaced with linearly interpolated values. No attempt was made to correct for near surface biases in radiosonde-measured temperature or humidity associated with heating/flow around the ship superstructure, though care was taken prior to launch to minimize this effect.

Once quality controlled, the sounding data were used to examine winds and thermodynamic data as a function of both time and height. First, a time series of convective available potential energy (CAPE), convective inhibition (CIN), mixed-layer wet-bulb potential temperature (θ_w), mean mixed-layer mixing ratio (MLMR), and vertical profiles of thermal buoyancy (e.g., θ_e of a parcel minus θ_{es} of the environment) were computed for each sounding. These computations utilized a pseudoadiabatic parcel representative of the lowest 50 hPa of the sounding (assumed to be the mixed layer). Second, a time series of deep tropospheric wind shear was constructed by computing the difference between layer mean meridional and zonal wind components in the 1–4-km and 9–12-km height layers. These layers approximately encompass the lower and upper levels of both deep convection and easterly wave disturbance structure observed during EPIC-2001.

Next, in order to study easterly wave phases and structure with height, the four sounding data were interpolated to 100-m height levels and examined in the time–height domain. To further smooth the data and account for missing levels, the 4-h data were then averaged to produce a time–height series of 24-h means. Further

TABLE 3. Number of samples composited per wave phase.

Phase/data	Ridge	North	Trough	South
Soundings	16	32	32	32
Surveillance scans	255	910	676	931
Volume scans	266	941	721	939
EVAD scans	16	9	47	29

isolation of easterly wave signals in observed and diagnosed sounding variables (e.g., temperature and humidity) was accomplished by bandpass filtering the 24-h means using a Gaussian high-pass filter, followed by a two-point running mean to emphasize signal possessing periods of 3 to 5 days. Other filtering schemes (Leise, exponential, running mean, etc.) yielded similar results.

Following the studies of Reed and Recker (1971), Burpee (1974, 1975), and Thompson et al. (1979), we relied heavily on the meridional (v) wind direction and speed at the 700-hPa level (mean height approximately 3160 m) to create a "composite" easterly wave. As a consistency check, we also compared the v wind-based technique with zonal winds and pressure–height trends at 700 hPa and surrounding levels. To ensure that an adequate number of soundings existed for each phase of the composite we utilized only four easterly wave phase categories as opposed to the eight categories used in previous studies (Reed and Recker 1971).

In order for data (radar, sounding, rainfall, fluxes, etc.) to be designated as occurring within a particular wave phase, the v wind direction and speed at 700 hPa in the *RHB* soundings were used as partitioning criteria. The four wave phases were defined as follows: *Ridge* (transition from southerly to northerly wind, $|v| < 2$ m s^{-1}); *North* ($v \leq -2$ m s^{-1}); *Trough* (transition from northerly to southerly wind, $|v| < 2$ m s^{-1}); and *South* ($v \geq 2$ m s^{-1}). The v wind speed threshold of 2 m s^{-1} represents approximately one standard deviation in the v wind speed distribution (spurious values removed), which possessed a mean of close to 0 m s^{-1}. Values used to create the sample distribution were taken from each sounding at heights occurring within a 500-m-deep layer centered on the height of the 700-hPa level. As a consistency check, the wind-based phase delineation was also compared to observed tendencies in daily pressure surface heights for levels between 850 and 500 hPa. Once the phases were determined, sounding thermodynamic and wind parameters were averaged at each 100-m level for each phase to create a composited easterly wave structure. The number of soundings used for compositing sounding parameters for each wave phase are indicated in Table 3.

b. RHB C-band radar data

Equivalent radar reflectivity (Z_e) and radial velocity (V_r) data collected by the *RHB* C-band radar were the primary variables utilized in this study. Prior to ana-

lyzing these data, some basic quality control measures were undertaken (in addition to daily receiver and solar calibrations conducted during the field campaign). First, comparisons of *RHB* Z_e were made with collocated pixels of calibrated S-band wind profiler data (R/V *Horizon*) and six overpasses of Tropical Rainfall Measuring Mission (TRMM) satellite precipitation radar (PR) data (for altitudes above the freezing level). In the mean, *RHB* Z_es degraded to the ~4 km footprint of the TRMM PR differed by less than 1–2 dB from the PR Z_e (M. Anagnostou 2001, personal communication). We arrived at a similar result when comparing collocated S-band profiler and *RHB* Z_e data for several volume scans when precipitation was located over the R/V *Horizon*. Finally, the raw radar data (both surveillance and volume scans) were reprocessed with TRMM ground validation quality control software to remove low-level second trip and sea-clutter echoes [courtesy Mr. D. Wolff, National Aeronautics and Space Administration (NASA) Goddard Space Flight Center (GSFC)].

Following the quality control checks/procedures, the Z_e data were gridded to a 1 km $\times$ 1 km $\times$ 0.5 km Cartesian grid spanning heights from 1 to 18 km above sea level using NCAR reorder software (Mohr 1986). The entire gridded Z_e dataset was then utilized to compute several quantities.

1) Rain rates for each pixel at the 1-km height level within 120 km of the 10°N, 95°W fixed point, at 10-min intervals: prior to computing rain rates, the Z_e data from each pixel in *RHB* surveillance scans at the 2-km height level were classified as either stratiform or convective based on a reflectivity texture algorithm (cf. Steiner et al. 1995; Rickenbach and Rutledge 1998). Briefly, the algorithm uses two criteria to classify a given Z_e pixel as convective or stratiform. The first criterion is based on a given Z_e exceeding a prescribed intensity or Z_e threshold. Based on previous studies (e.g., Rickenbach and Rutledge 1998), pixels were classified as convective if Z_e was ≥40 dBZ (note that all Z_e pixels in the grid column above and below are then also classified as convective). For pixels not exceeding the prescribed threshold, the second criterion used local gradients and relative maximums in the Z_e field (i.e., peakedness) to identify convective and stratiform precipitation (see Rickenbach and Rutledge 1998 for more detailed discussion). Following the stratiform–convective partitioning, rain rates for each pixel and scan time were computed from Z_e data using Z_e–R relationships for convective ($Z_e = 139R^{1.43}$) and stratiform rainfall ($Z_e = 367R^{1.30}$) derived for the western Pacific warm pool by Tokay and Short (1996). Due to uncertainty in the exact form of the Z_e–R relationship for this region of the Pacific Ocean (the subject of a current study), the radar-diagnosed rain rates used herein should be viewed only as a tool for making relative comparisons between different phases of the easterly waves.

2) Following computation of rain rates, all pixels at the 1-km level with rain rates ≥0.1 mm h^{-1} (~10 dBZ) were used to compute total, convective and stratiform rain-rate distributions, cumulative distributions of accumulation as a function of rain rate, and fractional rain volume contributions as a function of both time and wave phase.

3) To evaluate vertical structure changes in precipitation, 48-h running mean time–height series and easterly wave composites of mean Z_e, deviation from the mean Z_e, relative frequency of $Z_e \geq 20$, 30,[1] and 40 dBZ, and fractional area coverages (expressed as a percentage) of $Z_e \geq 20$ and 40 dBZ for each scan and wave phase were also computed. Pixels used in the computation of the mean, deviation and relative frequency statistics were included only if the pixel $Z_e \geq 0$ dBZ. In contrast, area fractional coverage distributions for each height were computed as the percentage of the entire sampling domain (i.e., all pixels within 120-km range of the *RHB* included) covered by echo greater than 20 and 40 dBZ at each 10-min scan.

4) The extended velocity azimuth display (Srivastava et al. 1986; Matejka and Srivastava 1991) technique was utilized to diagnose divergence and vertical air motion in selected radar volumes. The EVAD technique was applied to a total of 101 radar volumes characterized by nearly complete echo coverage surrounding the ship (maximum allowable azimuthal gap was 60°). These volumes contained 20–21 full Plan Position Indicator (PPI) elevation tilts with elevation angles ranging from 0.5°–60°. For vertical motion calculations, the top boundary where vertical air motion was assumed to be equal to zero was set 1 km above the highest velocity–azimuth display (VAD) analysis ring from the steepest elevation angle. This height offset was used based on results of previous studies indicating that the highest VAD analysis ring was often located 1 to 2 km below the actual height where vertical air motion was zero (Cifelli et al. 1996). Some caution should be applied in the interpretation of the vertical air motion profiles, since the upper-boundary location in these profiles cannot be independently confirmed and the number of volumes in each EVAD composite bin is relatively small (Table 3).

Table 3 indicates the number of radar surveillance, volume and EVAD scans used for creating rain rate and vertical structure composites for each wave phase.

---

[1] Reflectivities in excess of 30 dBZ are often used as a proxy for the presence of significant solid and/or liquid precipitation water content, and when observed at temperatures < -10°C have been previously associated with lightning producing cumulonimbus clouds in the Tropics (e.g., Zipser and Lutz 1994; Petersen et al. 1996).

c. Surface bulk flux data

The turbulent fluxes used in this study were computed using the Tropical Ocean Global Atmosphere Coupled Ocean–Atmosphere Response Experiment (TOGA COARE) bulk flux algorithm, version 3.0 (Fairall et al., 1996a,b, 2003). Inputs for the algorithm include wind speed, air temperature, humidity, and sea surface temperature. Wind speed was measured with a sonic anemometer and corrected for sensor motion (Edson et al. 1998) and flow distortion due to the *RHB* superstructure. Atmospheric temperature and humidity were measured with an aspirated Vaisala HMP 235 [0.1°C, 2% relative humidity (RH) quoted accuracy] and field checked against a handheld Assmann psychrometer standard; typical corrections for temperature and humidity were on the order of 0.2°C and 0.3 g kg^{-1}, respectively. Near-surface ocean temperatures were measured with a specially developed floating temperature sensor called a ''seasnake,'' which samples at a depth of about 5 cm. Downward radiative fluxes were measured using Eppley Laboratories precision infrared radiometer (PIR) and precision spectral pyranometer (PSP) sensors. Upward solar fluxes were computed assuming an albedo of 0.05, and upward IR fluxes were computed from sea surface interface temperature assuming an emissivity of 0.97. Mean flux values for each wave phase were determined by averaging an ensemble of 30-min mean values collected over the duration of the field campaign.

d. Satellite observations

In order to verify the approximate dates of easterly wave passage through the experiment domain and to assess the geographic origin of each easterly wave (e.g., Chang 1970; Reed and Recker 1971; Serra and Houze 2002), *Geostationary Operational Environmental Satellite-8* (*GOES-8*) infrared brightness temperatures (TBs) were used to develop time–longitude diagrams of TB and TB anomalies. This was accomplished by averaging TB values in 0.5° longitude bins from 50°W to 120°W (central Atlantic to east Pacific) over 24-h time intervals, for the latitude band of 5°N to 15°N. Brightness temperature anomalies for each day and 0.5° meridional bin were computed by subtracting the mean TB computed from the entire dataset for each bin (time period 5 September 2001 to 1 October 2001) from the mean TB computed for each bin and individual time, and then subsequently averaging these differences over 24-h periods to arrive at a daily mean TB anomalies. The TB data were subsequently bandpass-filtered (same technique as sounding data) to isolate the 2–7-day signal.

e. Lightning observations

Because easterly wave activity clearly modulates convective activity (Fig. 2) it is useful to examine simple

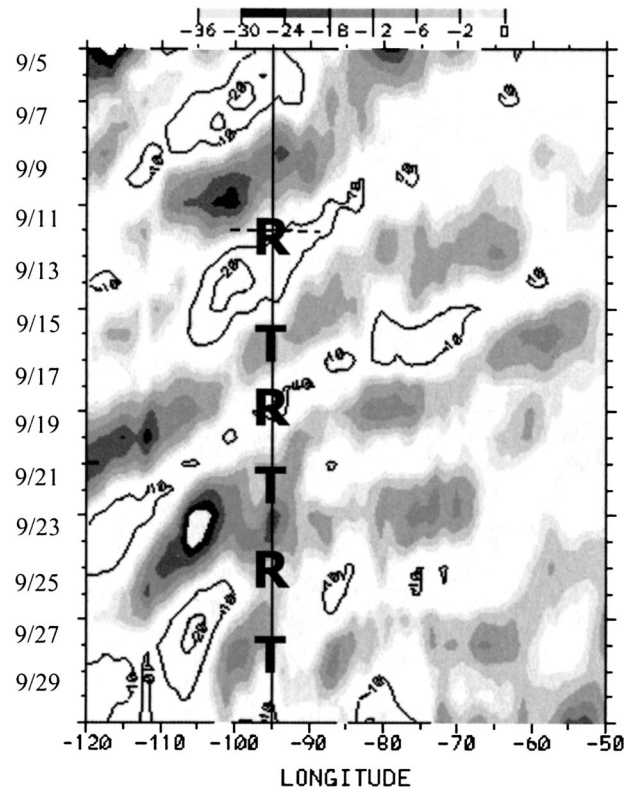### TB Anomaly 5°N - 15°N (9/5 – 10/01, 2001)

FIG. 2. Time–longitude plot (5 Sep–1 Oct 2001) of *GOES-8*-filtered IR brightness temperature anomalies (K) for latitudes between 5°N and 15°N. Cold anomalies are shaded; warm anomalies are contoured at 10-K intervals. Time begins on the ordinate in the upper left-hand corner and increases downward. Degrees of longitude are indicated on the abscissa with the meridional location of the *RHB* indicated by a vertical line at −95°. ''R'' and ''T'' indicate approximate times of ridge and trough passages, respectively. The horizontal dashed line at 12 Sep indicates the approximate start of on-station data collection by the *RHB*.

metrics of convective activity as an additional means for assessing changes in convective regime with time over a given area. One such metric is a simple count of lightning flashes over a given area as a function of time (e.g., Rutledge et al. 1992; Williams et al. 1992; Petersen et al. 1996; Nesbitt et al. 2000; Boccippio et al. 2000; Toracinta et al. 2002; Petersen and Rutledge 2001; Petersen et al. 2002). While no lightning detection sensors were deployed in and/or near the eastern Pacific domain of the EPIC-2001 field campaign, the long-range product of the National Lightning Detection Network (NLDN) does detect cloud-to-ground lightning flashes near and in the EPIC-2001 domain (e.g., Cramer and Cummins 1999). Though the detection efficiency of the NLDN is poor at the range of the experiment domain (10% or less), the data still provide a relatively unbiased qualitative measure of daily lightning activity. Hence the long-range NLDN data were utilized in daily time series form together with thermodynamic measures such
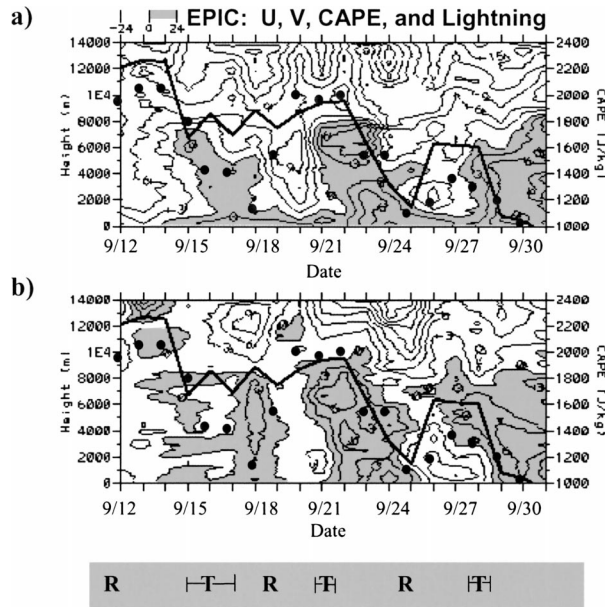
FIG. 3. Time–height (left ordinate) series of 24-h mean *RHB* sounding (a) *U* and (b) *V* winds for 12 Sep–1 Oct 2002 (positive values shaded). A time series of 24-h mean CAPE (solid line; smoothed) is plotted on the right ordinate. Black circles (●) are also plotted to indicate relative daily *trends* in CG lightning flash count (smoothed) that occurred within 150 km of the *RHB*. Approximate times of ridge (R) and trough (T) passages are indicated at the bottom.

FIG. 4. Time series of daily layer mean deep tropospheric shear [$\mathbf{V}_{9-13km} - \mathbf{V}_{1-4km}$] from *RHB* soundings for the zonal (ΔU), meridional (ΔV), and total shear ($\Delta U^2 + \Delta V^2)^{1/2}$. Approximate dates of ridge (R) and trough (T) passages indicated.

as CAPE and θ_w to further detect changes in convective regime that occur as a function of easterly wave phase.

4. Results

During the ITCZ leg of EPIC-2001 three distinct easterly wave passages occurred at the position of the *RHB* in intervals of approximately 5 days. Time–longitude diagrams of *GOES-8* TB anomalies (Fig. 2) suggest that the first two waves originated east of 50°W (images from the Tropical Prediction Center suggest West Africa as an origin). The origin of the third wave is not clear in the TB data, and is further complicated by cloudiness associated with Hurricane Juliette, which exited the northwest portion of the study area by 25 September. Juliette notwithstanding, after moving westward over Central America the easterly waves were easily detected in both sounding and radar data collected aboard the *RHB*. As indicated in Fig. 2, cold TB anomalies were typically observed near the time of trough passages and warm anomalies were generally observed in and behind ridges.

a. Time–height analysis of tropospheric wind and thermodynamic structure

Assuming uniform westward zonal phase velocity with height, a time–height series of both the *u* and *v* winds observed at the *RHB* (Figs. 3a,b) suggest that
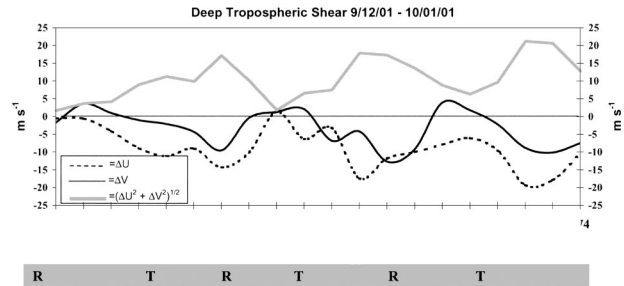
easterly wave passages possessed a westward phase tilt with height. This westward phase tilt is similar to that observed over the western Pacific (Reed and Recker 1971), the eastern Atlantic (Reed et al. 1977), and over the eastern Pacific 30°W of the EPIC ITCZ domain at 8°N, 125°W (Serra and Houze 2002). The positive correlation between the *U* and *V* wind components suggests equatorward transport of easterly momentum in the waves, and is consistent with at least some barotropic conversion of zonal to eddy kinetic energy.

Both theory and observations suggest that the location of maximum convective activity (measured by rainfall accumulation) may be related to the phase tilt with height of the easterly waves (e.g., Riehl 1954; Holton 1971; Reed and Recker 1971). For example, Reed and Recker (1971) observed increased convection and rainfall ahead of (behind) the trough axis in western Pacific easterly waves that tilted westward (eastward) with height. The conceptual model of a Caribbean easterly wave presented in Riehl (1954) tilted eastward with height and most of the convective activity and rainfall occurred east of the trough axis. In relation to the aforementioned studies of wave tilt and phasing with convection and rainfall, Figs. 3a,b indicate that just prior (0–2 days) to the passage of each 700-hPa wave trough (e.g., transition from northerly to southerly flow), values of CAPE and cloud-to-ground (CG) lightning flash count exhibited *relative* maximums. As we shall demonstrate in section 4c, the higher-frequency (3–5-day periods) trends in conditional instability and lightning apparent in Figs. 3a,b, indicate the presence of more vertically developed convection just prior to the passage of the wave troughs in weak northeasterly flow.

Consistent with the westward tilt of the waves in Figs. 3a,b, and as expected via the theoretical study of Holton (1971) and observational studies of Reed and Recker (1971), Reed et al. (1977), and Serra and Houze (2002), the deep tropospheric shear was east-northeasterly during the ITCZ leg of EPIC (Fig. 4). While the observed wave tilt with height can be explained dynamically by the presence of diabatic heating in a sheared flow, the potential upstream interaction of the easterly waves with topography located 500–1000 km east of the EPIC do-
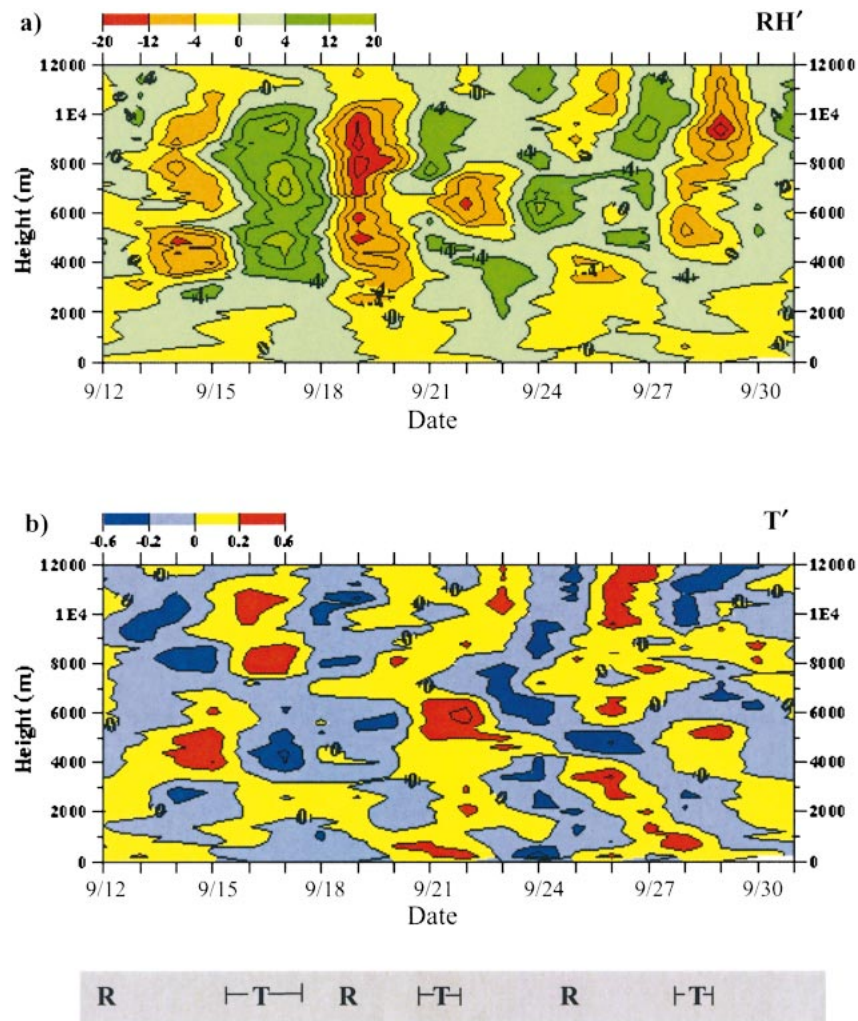
FIG. 5. Time–height series of bandpass-filtered (2–7 day) (a) relative humidity anomalies (RH′) with contour interval of 4%, and (b) temperature anomalies (T′) with contour interval of 0.2°C. Approximate time of ridge (R) and trough (T) axis passages also indicated.

main could also play a role in producing the observed wave tilt (e.g., Zehnder et al. 1999).

From a temporal perspective, peaks in the magnitude of the northeasterly shear tended to occur 2–3 days behind the passage of the trough axis when southerly flow was present at 700 hPa. The weakest shear was found in the northerly phase at 700 hPa, to the east (west) of the ridge (trough) axis, which coincided with periods of largest instability and more CG lightning (Figs. 3a,b). This suggests that less organized, but more vertically erect convection might preferentially occur to the west of the wave trough axis in northerly flow. The overall temporal trend in the shear, as a function of easterly wave phase during EPIC, seems broadly consistent with the results of Serra and Houze (2002) for the eastern Pacific domain of the Tropical Eastern Pacific Process Study (TEPPS; Yuter and Houze 2000).

Tropospheric perturbations in relative humidity (RH′;

specific humidity trends very similar) and temperature (T′) associated with the easterly wave passages were most apparent in the *RHB* sounding data after bandpass filtering the data to isolate signals with 2–7-day periods (Figs. 5a,b). Maximum RH deviations were on the order of 10%–20% and occurred primarily in the mid- to upper troposphere. Note that the *filtered* perturbations in RH in the lowest 2 km of the troposphere were generally quite small, <2%. However, as evinced in Fig. 6 (and similar to the western Pacific warm pool; Petersen et al. 1996), relatively small changes in the nonfiltered boundary layer moisture [e.g., 0.5 g kg^{-1}, O(3% RH)] resulted in small but well-correlated changes in boundary layer θ_w (0.4°C), and relatively *large* changes in CAPE (400 J kg^{-1}) and lightning flash count (e.g., Figs. 3a,b).

Though noisy, time–height trends of RH′ and T′ (Figs. 5a,b) do exhibit some systematic behavior. For example, at upper levels (between 8 and 10 km, ~400–
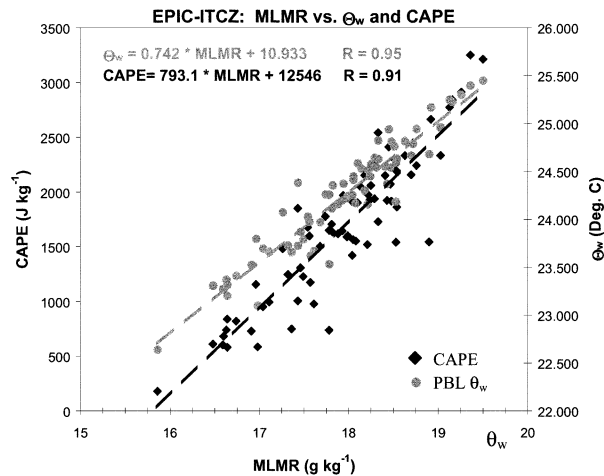
FIG. 6. *RHB* sounding values of MLMR (abscissa) vs CAPE (black; left ordinate) and mixed-layer θ_w (gray; right ordinate). Also shown are equations for the best-fit lines and linear correlation coefficients (R) of the fit for each relationship.

300 hPa) near the time of trough passages (during and after in the first two instances, 1 day before in the last) there is some evidence for coincident warming and moistening (positive RH′), indicating the possible presence of convective heating (advection is also a possibility) and the creation of eddy available potential energy. There is a persistent decrease in mid- to upper-level RH (4–12 km) that also tends to occur between the first two ridge and trough axis passages during periods of deep east-northeast flow (Figs. 3a,b) and during the third trough passage in east-southeast flow aloft. At midlevels (4–6 km, ~600–500 hPa) there is a slight hint of warming that occurs in the vicinity of the trough axis (either just prior to 14–15 September or during 21 and 29 September). Approximately 2 to 3 days behind the first two trough passages, a cooling and moistening signal is present at midlevels (e.g., days 260 and 266; also inferred from increases in specific humidity). At low levels (height < 1 km), the only persistent features in the filtered data were slight warming (Fig. 14b later) and a small increase in specific humidity (not well reflected in RH′) between the ridge and trough passages.

b. Radar-diagnosed rainfall and wave phase

Not surprisingly, perturbations in tropospheric momentum and thermodynamic structure associated with the easterly waves discussed in section 4a were also associated with corresponding changes in rainfall amount, rain rate, and the vertical structure of convection. For example, there were clear increases in the contribution (approaching 90%–95% of the total rain volume; Fig. 7a) to area mean rainfall by radar pixels classified as "convective" just before and during the trough passages. Conversely, stratiform contributions to the total rain volume (typically ≤20%) tended to peak 1 to

3 days after trough passages. Indeed, when integrated over the entire field campaign, stratiform precipitation contributed only 15% of the total rain volume, while convective precipitation accounted for approximately 85%. These numbers differ from previous statistically based (e.g., inclusion of numerous raining systems) sea and/or space-based radar studies of stratiform and convective precipitation over other tropical oceanic locations, which indicate typical stratiform (convective) contributions to total rainfall of 30%–50% (50%–80%; e.g., Cheng and Houze 1979; Tokay and Short 1996; DeMott and Rutledge 1998a; Rickenbach and Rutledge 1998; Berg et al. 2002).

When considered from an area coverage perspective in addition to the convective–stratiform partitioning, further systematic behavior in precipitation behavior relative to easterly wave phase becomes apparent. For example, time series of heavy (≥25 mm h^{-1}) and light (≤5 mm h^{-1}) rain-rate area coverage are illustrated in Fig. 7a. Note that larger areas of heavy rain (convective in origin) tended to precede the passage of easterly wave troughs by approximately 0 to 2 days. Conversely, areas of light rain (typically 100 times larger in area coverage than heavy rain areas) including *both* convective and stratiform precipitation components tended to peak 1 to 2 days behind wave troughs, with the exception of the last event (27–28 September; Fig. 7a).

At first glance, the area mean rainfall trend in Fig. 7a seems to exhibit only a weak correlation with wave phase, sometimes peaking prior to (e.g., 13 September and 26–27 September), and sometimes peaking during or after passage of the wave trough (e.g., 16 September, 23–24 September). However, relative peaks in the area mean rainfall and the area coverage of heavy convective rain do exhibit temporal coherence and are reasonably well correlated, particularly for periods when area mean rainfall peaked prior to trough passage (e.g., 13, 20, and 26–27 September). The influence of large areas of light convective and stratiform rain on area mean total rainfall is also evident on 16–17 September and 23–24 September in Fig. 7a. During periods when the light rainfall area peaked (e.g., posttrough and even into the ridge phase) the fraction of stratiform rain increased in two events (17 and 24 September). However, as inferred from the trend in convective rain fraction, light convective rain rates always dominated the rainwater volume contribution as a whole (Fig. 7a).

While previous studies of AEWs (Hudlow 1979; Reeves et al. 1979; Thompson et al. 1979) suggest that a stronger temporal correlation should exist between the area mean precipitation and wave phase, the limited EPIC ITCZ field campaign sample size (e.g., three wave passages), combined with the scale of the rainfall measurement area, the relative organization of each easterly wave, and the occurrence of other mesoscale/synoptic-scale phenomena, could easily account for noise in the rainfall–wave phase trends shown in Fig. 7a. For example, the peak in total rainfall occurring just prior to
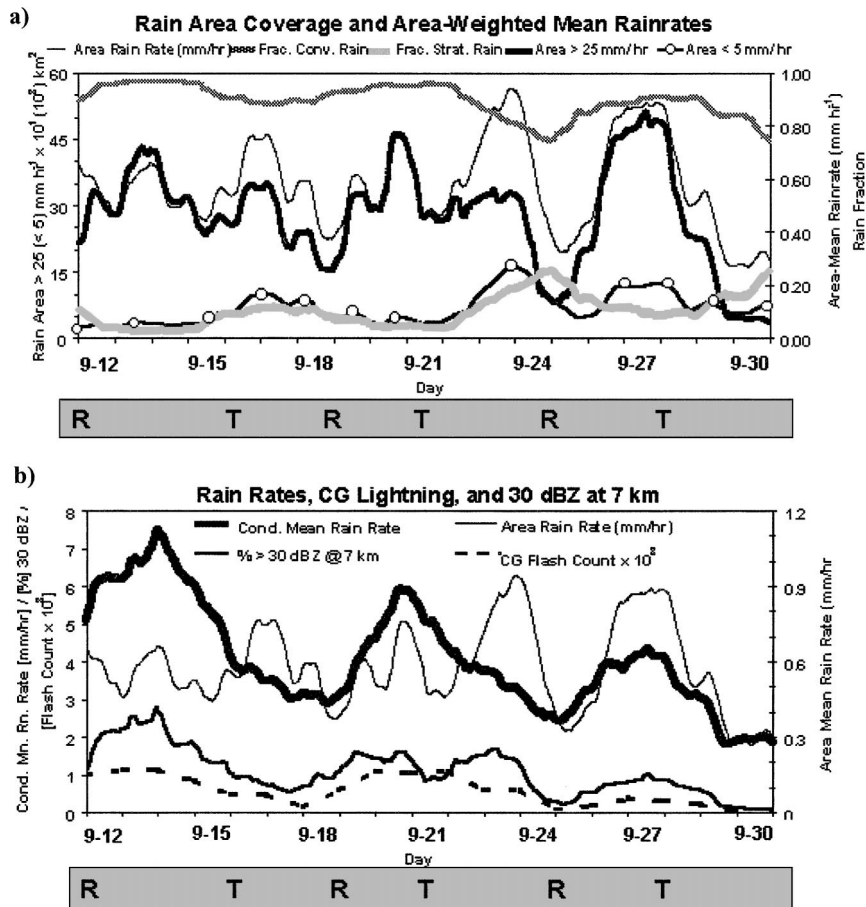
FIG. 7. Time series of 48-h running mean: (a) areas of rain rate ≤ 5 mm h^{-1} and ≥ 25 mm h^{-1}, left ordinate; area mean rain rate (mm h^{-1}), right ordinate, convective and stratiform rain volume fractions and (b) conditional mean rain rate (mm h^{-1}), CG lightning flash count $\times 10^3$, percentage of reflectivity ≥ 30 dBZ at 7 km (left ordinate); and area mean rain rate (mm h^{-1}) plotted on the right ordinate. Ridge (R) and trough (T) passages indicated at the bottom.

the ridge phase on 22–24 September may have been forced in part by interaction of lingering bands located along the periphery of Hurricane Juliette (~550 km northwest of the *RHB* on 22 September) with the environment in the vicinity of the *RHB*. Noisy rainfall data notwithstanding, the periodicity of easterly waves can be still be discerned from the relative peaks in the total rain-rate time series.

Compared to the area mean rain rate, one rain-rate statistic that exhibits stronger coherence with the easterly wave signal is the conditional mean rain rate (Fig. 7b). Recall that the *conditional* mean rain rate represents the average rain rate observed at each scan time computed from the reduced sample of only the raining pixels (≥ 0.1 mm h^{-1}); it is a measure of the mean rain intensity over only the raining areas. To the extent that modulation of the synoptic-scale environment influences the physical characteristics of precipitation production, which in turn control the rain rates in convective-scale events (e.g., areas of heavy convective rain), we except

to observe some coherency between conditional mean rain rates and wave phase.

Indeed, the physical connection between modulation of convection by easterly wave phase and conditional mean rain rate is clearly evinced in the data of Figs. 7a,b by noting that the relatively small areas of heavy convective rain occurred coincident with peaks in conditional mean rain rate (Fig. 7b) prior to trough passages. Further, Fig. 7b suggests that conditional mean rain rates were highly correlated to the percent echo exceeding 30 dBZ at the 7-km level ($-12°$C), which comprised 1%–3% of the echoes with $Z_e \geq 0$ dBZ. Conditional mean rain rates were also positively correlated to daily CG lightning flash counts. Collectively, these results (Figs. 7a,b) suggest that a significant precipitation ice phase existed in at least a small fraction of the clouds (e.g., Goodman et al. 1988; Dye et al. 1988; Zipser and Lutz 1994; Petersen et al. 1996; Carey and Rutledge 2000; Petersen and Rutledge 2001) during peaks in conditional mean rain rate, heavy rain area,
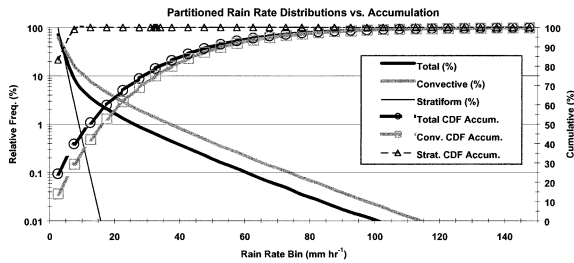
FIG. 8. Radar-diagnosed relative frequency distributions of rain rate on the left ordinate, and cumulative distributions of rain accumulation cumulative distribution function (CDF) as a function of rain rate on the right ordinate for total, convective, and stratiform rain components.

and CG lightning just prior to wave trough passage (peak on 23 September in 30-dBZ coverage excepted, Fig. 7b). Note that trends in the conditional mean rain rate do not always correlate well to area mean rain rates, reflecting the importance of both temporal variability in echo coverage area and the distribution of rain rates.

Distributions of rain rate and rain accumulation (Fig. 8) suggest that ~50% of the accumulated rainfall measured by the *RHB* radar during EPIC-2001 was produced by the upper 5% of observed rain rates (i.e., rain rates ≥ 15 mm h^{-1}). The distribution of rain rates for total, convective and stratiform rain shown in Fig. 8 clearly indicate that rain rates >10–15 mm h^{-1} were predominantly convective in origin (cf. Austin and Houze 1972; Steiner et al. 1995). Indeed, accumulations associated with "heavy" rain-rate areas (≥ 25 mm h^{-1}; Fig. 7a) accounted for more than one-third of the total accumulated rainfall, even though these regions only covered 1% of the area typically covered by light rain (≤ 5 mm h^{-1}). Note that the lighter rain rates (making up nearly all of the stratiform rain-rate distribution and ~50% of the convective rain-rate distribution) only accounted for approximately one-quarter of the total rainfall (Fig. 8).

When partitioned into convective and stratiform components, it is clear from Fig. 8 that convective contributions to the total rain accumulation were dominant in the vicinity of the *RHB,* with ~50% of the convective rain accumulation associated with rain rates in excess of 20 mm h^{-1} (the upper 5%–7% of the convective rain-rate distribution). Since precipitation is a measure of integrated latent heat release in the atmospheric column, these results emphasize the importance of convective-scale contributions in the energetics of synoptic-scale phenomena. While large areas of light precipitation (consisting of both weak convective and stratiform rain, observed in or behind the wave troughs) are undoubtedly important to the diabatic heating budget of easterly waves, the much smaller areas of heavy convective rainfall leading the wave troughs, and those embedded within the lighter rain areas clearly make a significant contribution to the total diabatic heating.
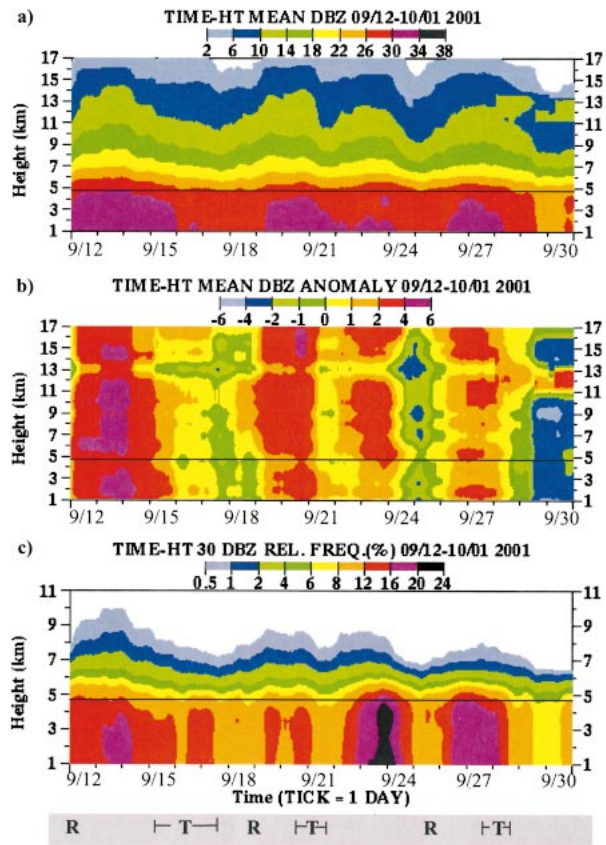

FIG. 9. Forty-eight-hour running mean time–height cross sections of *RHB* (a) conditional mean radar reflectivity (dBZ), (b) deviation of reflectivity from the conditional mean (dB), and (c) relative frequency of reflectivity ≥ 30 dBZ (%). The height of 0°C level is indicated by the thin black line, and the approximate timing of ridge (R) and trough (T) passages is also indicated.

c. 4D convective structure and wave phase

From an Eulerian frame of reference, the aforementioned behaviors of conditional mean rain rate, rain area, and CG lightning flash count (Figs. 7a,b) all suggest concomitant systematic changes in the vertical structure and coverage of convection as a function of easterly wave phase. Time–height series of the conditional mean Z_e, deviation from the mean Z_e and the relative frequency of 30-dBZ echo (Fig. 9a–c), all suggest that there is a higher probability of more intense, vertically developed convection 1 to 2 days ahead of (behind) the trough (ridge) axis. For example, the mean reflectivity profile at each time (Fig. 9a) exhibits a systematic increase prior to the passage of each wave trough, and a relative decrease during ridge passages. These increases and decreases in Z_e are particularly evident in the Z_e deviation patterns (Fig. 9b) where there seems to be a slight indication that Z_e exhibits more persistent increases above the freezing level in association with the trough passages. Consistent with the aforementioned increases in lightning activity (Figs. 3, 7c) and conditional
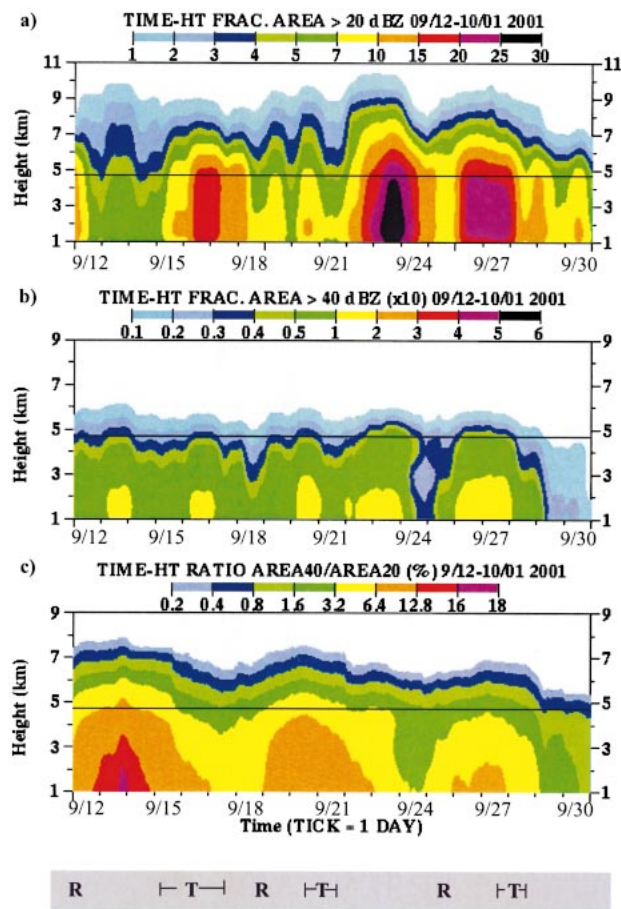
FIG. 10. As in Fig. 9, but (a) percentage of scan area covered by reflectivity ≥20 dBZ; (b) as in (a), but reflectivities ≥40 dBZ—note that the percentages in (b) have been scaled by a factor of 10; and (c) ratio/percentage of ≥20-dBZ area covered by reflectivities ≥40 dBZ.

erage at all height levels tends to occur coincident with or behind trough passages in the first two events (e.g., 16–17 September and 22–24 September—though hurricane Juliette may have influenced the signal on these days), and both before and after the last event (e.g., 27–29 September). However, when echo coverage at the higher threshold is considered (Fig. 10b), we note peaks in area coverage (especially at lower height levels) that also occur on three occasions ahead or on the leading edge of the trough axis (e.g., 13, 20, and 26–27 September). If the ratio of 40-dBZ echo coverage to that of 20-dBZ coverage is computed (Fig. 10c), a systematic trend in rain system convective intensity becomes apparent that is consistent with the heavy convective rain area trends discussed for Figs. 7a,b. As in Fig. 7a, Fig. 10c clearly delineates the heavy precipitation phase of the easterly waves, but further emphasizes the connection to vertical structure illustrated in Figs. 9a–c.

The distinction between "vertical development" and "area coverage" is an important one, as the two terms are often used as metrics of convective "intensity" depending on the application. For example, a time series of radar-derived "convective intensity index" (a measure of precipitation *area* coverage, though not amount, for precipitation rates exceeding ∼0.5–1 mm h^{-1}) presented in the easterly wave study by Serra and Houze (2002) suggests that convection is more intense (i.e., more widespread) in southerly flow found within or behind easterly wave trough axes in the eastern Pacific. Similarly, R03 found that more widespread convection occurred during EPIC-2001 in surface southwesterly flow (presumably in or behind a trough axis), based on airborne radar detection of *area mean* precipitation combined with *area mean* IR brightness temperatures. Note that the metrics of convective intensity in the Serra and Houze (2002) and R03 studies are, for the most part, a reflection of precipitation *area coverage,* as opposed to precipitation *vertical structure,* the measure of convective intensity emphasized in this study. Importantly, the EPIC-2001 results presented in Figs. 7–10 provide a more complete picture of convective structure trends enabling reconciliation of both vertical structure and/or area coverage interpretations of convective intensity. That is, *deeper,* more vertically developed convection covering a smaller total area, accompanied by ice-based precipitation processes, lightning, and heavy convective precipitation was *more likely* to lead the trough phase of the easterly waves sampled during EPIC-2001. Conversely, more widespread convection with light to moderate precipitation (convective and stratiform components) and relatively weaker vertical development tended to follow the trough phase (consistent with Serra and Houze 2002 and R03).

5. Composited easterly wave structure

As demonstrated in numerous earlier studies (Reed and Recker 1971; Burpee 1974; Reed et al. 1977;

instability (Fig. 3), Fig. 9c clearly demonstrates a peak in the percentage of deep and vertically developed convective cells prior to wave trough passage, followed by a general decrease in this percentage entering the ridge phase. Finally, note that the aforementioned changes in convective vertical structure are consistent with previously discussed changes in the time series of mean conditional rain rate, cloud-to-ground lightning, and heavy convective rain area.

As a complement to the aforementioned vertical structure observations it is useful to examine time–height echo *area* coverage distributions (i.e., the percentage of area covered by an echo of given threshold within 120-km range of the *RHB*). To do this we consider the fractional area coverage for two thresholds, one threshold set at 20 dBZ (mixture of stratiform and convective rain rates of ∼0.5–1 mm h^{-1}; Figs. 8, 10a), and the other set at 40 dBZ (convective rain rates ∼20–25 mm h^{-1}; Fig. 10b). In Fig. 10a the largest ≥20-dBZ echo cov-

Thompson et al. 1979) an efficient way to describe the combined behavior of easterly wave thermodynamics, kinematics, and rainfall is to create a composite wave structure for several key parameters as a function of phase and height. Herein we create similar composites as a means to consolidate the time series observations of section 4 into a cohesive, comprehensive, multidimensional view of eastern Pacific easterly waves as observed during EPIC-2001.

a. Wind structure

As in Fig. 3, the zonal and meridional wind components (Figs. 11a,b) are positively correlated and tend to tilt slightly westward with height indicating that, with westward movement of the wave, the trough axis at midlevels slightly precedes that at the surface. Consistent with the westward tilt (Holton 1971), strong tropospheric northeasterly shear is evident behind the trough, as a core of strong northeasterly winds (~20 m s^{-1}) above the 10-km level emerges in the southerly phase with coincident low- to midlevel southwesterly flow. The shear is weakest but still easterly during the northerly phase of the wave. Note that, in the mean, the easterly flow increases with height and the flow aloft (at altitudes above 10 km) exceeds 10 m s^{-1}. Given that easterly waves moved on average at speeds of 6–8 m s^{-1} toward the west, in the reference frame of the easterly waves, the air at upper (lower) levels moves from an easterly (westerly) direction similar to that observed in AEWs during the Global Atmospheric Research Program (GARP) Atlantic Tropical Experiment (GATE; Thompson et al. 1979).

b. Thermodynamic structure

Temperature and humidity anomaly patterns reflect consistent changes as a function of wave phase (Figs. 11c–e). Prior to the trough phase in low-level northerly flow there is a tendency for low-level warming and upper-level cooling to occur. While there is little net change in low-level (height ≤ 1 km) relative humidity across the wave phases due to warming, there are in fact slight increases in moisture (0.2–0.4 g m^{-3}) evinced in the specific humidity (Fig. 11e). At mid- to upper levels, definite drying is present during the ridge and northerly phases. Traversing the trough, a slight warming and moistening tends to occur from mid- to upper levels in and behind the trough in southerly flow while cooling occurs in and behind the trough at low levels in southerly flow. Note that these patterns are quite similar to those observed by Reed and Recker (1971; and modeled by Holton 1971) for westward-tilting easterly waves in the western Pacific, and those found in Lau and Lau (1990) for both the eastern Atlantic and western Pacific. Further, if we allow for a typical southwest to northeast tilt of the wave troughs in the horizontal plane (not shown, but present in field campaign analyses) and

consider the composited temperature (Fig. 11c) and wind fields (Figs. 11a,b), the presence of a thermal wind balance is also evident as found in previous studies of western Pacific easterly waves (e.g., Reed and Recker 1971).

Height and phase trends in the temperature and humidity anomaly fields (Figs. 11c–e), and implied virtual temperature anomalies (not shown), suggest the presence of 1) increased conditional instability (e.g., CAPE; Table 4) in the northerly phase ahead of the trough, 2) decreased instability in the southerly and ridge phases behind the trough, and 3) identifiable mid- to upper-level warming and moistening associated with convection in the trough and southerly phases. The effect of the thermodynamic anomalies on conditional instability (and hence convection) can be evaluated by examining a phase–height plot of parcel buoyancy (difference between parcel θ_e and that of the saturated environment θ_{es}) and values of CAPE (Table 4).

The most striking feature in the plot of buoyancy in Fig. 12 is the depth and magnitude of the conditional instability present in the northerly phase (mean CAPE $\sim$ 2000 J kg^{-1}, CIN $\sim$ 5 J kg^{-1}) (Table 4). Note that relative to the other wave phases, the shape of the buoyancy profile exhibits a rapid increase at low levels and a broad midlevel maximum that extends from near the freezing level (~4.5 km) to 8.5 km. There is also a clear suggestion of increased equilibrium height level during the northerly phase. The observed buoyancy profile and CAPE that occurs prior to the wave trough passage is consistent with the aforementioned presence of deep, vertically developed, lightning-producing convection during the pretrough phase (Figs. 9 and 10). The preference for larger CAPE in the northerly pretrough phase for the EPIC-2001 domain is also similar to that observed for AEWs over the eastern Atlantic Ocean (e.g., Thompson et al. 1979).

In the mean, the enhanced buoyancy profile and associated equilibrium heights extend somewhat into the trough phase (CAPE 1800 J kg^{-1}), but a marked stabilization occurs in the southerly regime. The lowest CAPE occurs during the ridge phase (Table 4); however, the CIN also decreases. Hence the ridge-phase stability profile suggests the potential for a plentiful, but comparatively weaker, population of convective clouds (discussed in section 5c and evinced in Figs. 9, 10, and 13). The convective fraction of this cloud population may in some sense be analogous to the eastern Atlantic AEW ridge-phase intermediate convective cloud-height population postulated by Thompson et al. (1979), or the trade/melting-level inversion-topped conjestus population observed by Johnson et al. (1999) for suppressed periods over the western Pacific warm pool. It is important to note, however, that regardless of easterly wave phase, there were always shallow precipitating clouds present in some fraction over the observational domain (as observed by scientists on board the *RHB*).
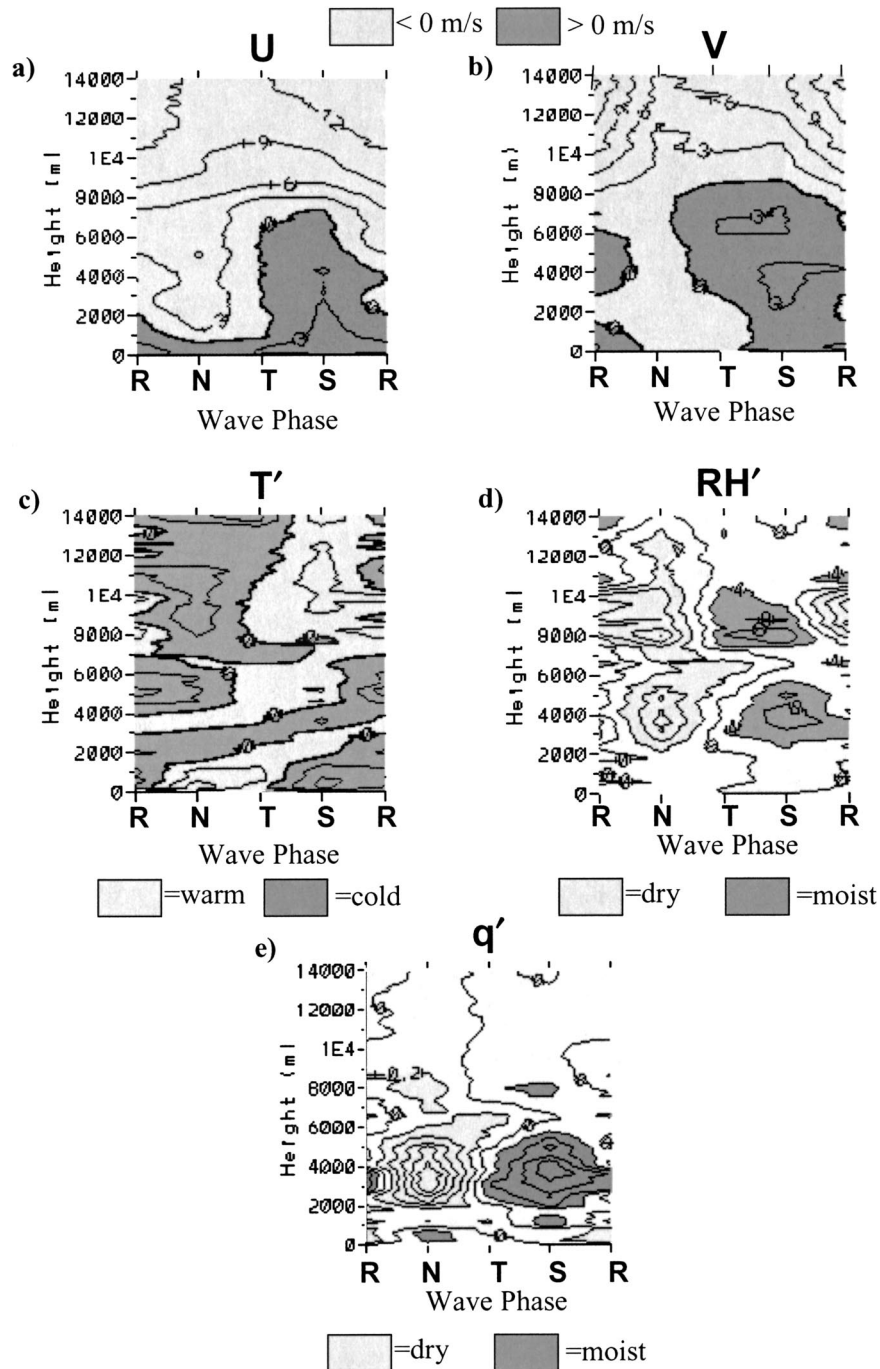
FIG. 11. Easterly wave composites for ridge (R), northerly (N), trough (T), and southerly (S) phases of (a) u (contour interval is 3 m s^{-1}); (b) as in (a), but v; (c) temperature anomaly (T' in °C, contour interval is 0.2°C); (d) relative humidity anomaly (RH$'$, in %, contour interval is 4%); and (e) specific humidity anomaly (q', g m^{-3}, contour interval is 0.2 g m^{-3}).

c. Vertical development versus area coverage

The time–height series of radar-diagnosed vertical structure and area coverage (Figs. 9 and 10) combined with the composited thermodynamic profiles shown in Figs. 11 and 12 hint at important differences in the modes of convection as a function of wave phase. These differences become apparent when easterly wave composites of the frequency of *RHB* radar reflectivity ≥30 dBZ (Fig. 13a) and the area coverage of reflectivity ≥20 dBZ (Fig. 13b) are created. For example, consistent with the buoyancy profiles (Fig. 12) and CAPE trends (Table

TABLE 4. EPIC ITCZ CAPE as a function of easterly wave phase.

Easterly wave phase	CAPE/CIN (J kg^{-1})
Ridge	1200/6
North	2000/5
Trough	1800/11
South	1400/11

FIG. 12. Composite easterly wave buoyancy ($\theta_{ep} - \theta_{es}$) as a function of height for ridge (R), northerly (N), trough (T), and southerly (S) wave phases. Buoyancy < 0 is shaded dark. Relative humidity ≥75% is indicated by light shading.

4), a deeper, more vertically developed population of convective clouds is clearly present in the northerly phase of the easterly waves (Fig. 13a) as evinced by the "tail" of 30-dBZ frequency that extends to heights exceeding 11 km. Further, the peaks in conditional mean rainfall rate and heavy convective rain area suggested in Figs. 7a,b are also evident when considering the relative difference in 30-dBZ frequency between northerly and adjacent phases. Note that there is actually a higher frequency of 30-dBZ reflectivity at lower height levels during the ridge phase than in either the trough or southerly phases, yet there is also a tendency for a 30-dBZ frequency "cutoff" near 7 km during the ridge phase (Fig. 13a). This is consistent with (a) the ridge-phase buoyancy profile in Fig. 11, which suggested the presence of a raining, but less vertically developed convection category; and (b) periods of dissipating stratiform rain, suggested in Fig. 7a by an increased fraction of stratiform rainfall. During the trough and southerly phases, Fig. 13a suggests that a population of deep convective clouds is present (again, consistent with Fig. 12), but at altitudes ≥6.5 km the echoes are approximately one-half as likely to contain echoes ≥30 dBZ relative to the northerly phase.

Similar to section 4c, we can also examine how much area the convection and rainfall actually cover, or equivalently, the probability of finding significant precipitation in a given sample area. This probability is represented in Fig. 13b by plotting the mean area of echo exceeding 20 dBZ at each height within a fixed radius of 120 km from the *RHB* radar as a function of wave phase. In stark contrast to Fig. 13a where the vertical convective structure of the northerly phase clearly dominates that of the trough and southerly phases at all heights, it is the trough and southerly phases that dominate the area of significantly raining echo coverage for heights ranging from the surface to 4 km [Fig. 13b; analogous to, but not exactly the same as the convective index trends discussed in Serra and Houze (2002)]. However, once the 20-dBZ areas extend above the 7-km level, the dominance of northerly phase convective vertical intensity suggested in Fig. 13a begins to reveal itself in area coverage as well, as does the overall reduction in deep cloud population in the ridge phase.

6. A summary of wave composite properties

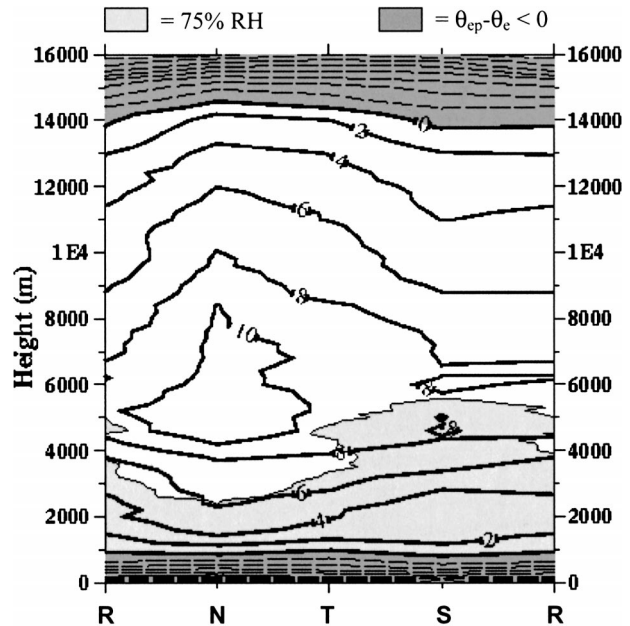The properties of eastern Pacific easterly waves observed during EPIC-2001 as related to convection, rain-

fall and surface moist entropy fluxes can be described in composite form with the aid of Figs. 14a–e.

1) CAPE (or alternatively mixed-layer θ_w, both of which are strongly correlated to MLMR; Fig. 6) and parcel equilibrium levels peak during the northerly phase prior to passage of the wave trough (Table 4, Fig. 14a). CIN reaches a relative minimum during the northerly and ridge phases. Though not shown here (but implicit in Fig. 4), deep tropospheric shear is at a minimum during the northerly phase and at a maximum behind the trough in the southerly phase.

2) The corresponding response of the convection and rainfall to trends in instability and shear is to exhibit deep vertical development, more lightning and a robust precipitating ice phase (Fig. 14b), larger heavy rain areas, and higher conditional mean rain rates during the northerly phase (Figs. 14c,d). This is followed by an overall reduction in the vertical intensity (Fig. 14b) and conditional mean rain rates in convection during the trough and southerly phases (Fig. 14c,d), but a corresponding increase in light convective and stratiform rainfall (Fig. 14c). Though not directly observed, it may be that widespread ascent sustained more widespread stratiform and weak convective precipitation coverage in the trough (e.g., Reeves et al. 1979), followed by slow dissipation in the southerly and ridge phases. Note that a significant fraction of the light precipitation during the composite ridge phase was associated with the single widespread precipitation event of 23–24 September (which was influenced by the presence of Hurricane
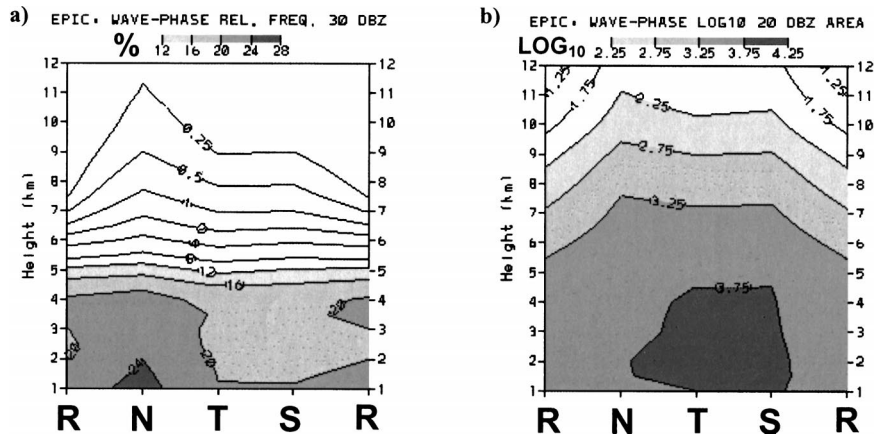
FIG. 13. Easterly wave composites of (a) relative frequency (%) of reflectivity $\geq$30 dBZ; and (b) $\log_{10}$ of echo coverage area $\geq$20 dBZ for ridge (R), northerly (N), trough (T), and southerly (S) wave phases.

Juliette). If this event were eliminated from the sample, the peak in composited light rain area coverage would occur during the trough and southerly phases.

3) The area mean rainfall, which behaved less systematically than conditional mean rain rates and area coverage in time series form (Figs. 7a,b), exhibits a broad peak centered over the trough phase in Fig. 14c. If rain-rate frequency and rainfall cumulative distributions are examined as a function of phase, systematic fine structure in the contribution to area mean rainfall as a function of phase becomes more apparent (Fig. 14d). For example, moving west to east across the wave trough, convective rain rates are heavier (lighter) in the northerly (southerly) phase, with 50% of the accumulated rainfall associated with rain rates $\geq$25 (10) mm h^{-1}. Importantly, though the convective rain-rate distributions vary by wave phase, absolute departures of the area mean rainfall in each phase differ from the 21-day mean ($\sim$13 mm day^{-1}) by only 10%–15%. Combined with aforementioned changes in convective structure observed to occur across the wave trough (Figs. 7, 9, 13, and 14b), the radar data suggest that net latent heat release of the same order of magnitude can occur across easterly waves, but the vertical profile of latent heat release is likely to be systematically different from phase to phase. Hence, the dynamic feedback of the convection to the synoptic scale should also be different in different phases of the wave.

4) Through *RHB* surface flux data were collected by a single platform, in relation to points 1 and 2 above, the data suggest that latent heat fluxes (Fig. 14d) increase in the widespread echo coverage behind the trough passage and peak in the ridge phase (when near surface winds were the strongest; Figs. 11a,b). The behavior of the latent heat fluxes seems broadly consistent with the CRM results of Xu and Randall (2001) and also the observational results of R03. Boundary layer moisture and CAPE do not begin to

recover (Fig. 14a) until convective coverage decreases in the southerly and ridge phases (Fig. 14c) followed by the storage of the latent heat between the ridge and northerly phases. The result of this cycle is a coincident peak in MLMR and CAPE during the northerly phase (Fig. 14a), which is then steadily depleted via convection through the northerly, trough and southerly phases. As in the case of the Madden–Julian oscillation, it may be that latent/sensible heat fluxes and boundary layer recovery in easterly waves are influenced by changes in the dominant mode of convective organization characteristic of each phase (e.g., Saxen and Rutledge 1998). Finally, note that, in addition to latent heat fluxes, combined heating via solar and sensible heat fluxes (sensible heat fluxes peaking during the preceding ridge phase) with enhanced tropospheric IR loss (inferred from northerly enhanced surface IR loss, increased solar gain, and reduced convective coverage) in the northerly phase would also act to increase the CAPE in the convective environment of the northerly phase (e.g., through lower-tropospheric warming and mid- to upper-tropospheric cooling as in Fig. 11c).

Finally, we can use the radar velocity information and EVAD technique to obtain an estimate of the mean divergence and vertical motion profiles characteristics of convective systems observed in each wave phase (Figs. 15a,b). Even with the relatively small samples available (especially in the ridge and northerly phases; Table 3), the profiles of mean divergence (Fig. 15a) and upward motion (Fig. 15b) are broadly consistent with the previous interpretations of both the buoyancy and convective structure in each phase. During the northerly phase the convective systems exhibited deep convergence extending from the surface to nearly 7 km, accompanied by upper-level divergence above 6 km. This resulted in deep upward motion throughout the vertical profile (Fig. 15b). A transition to more enhanced midlevel conver-
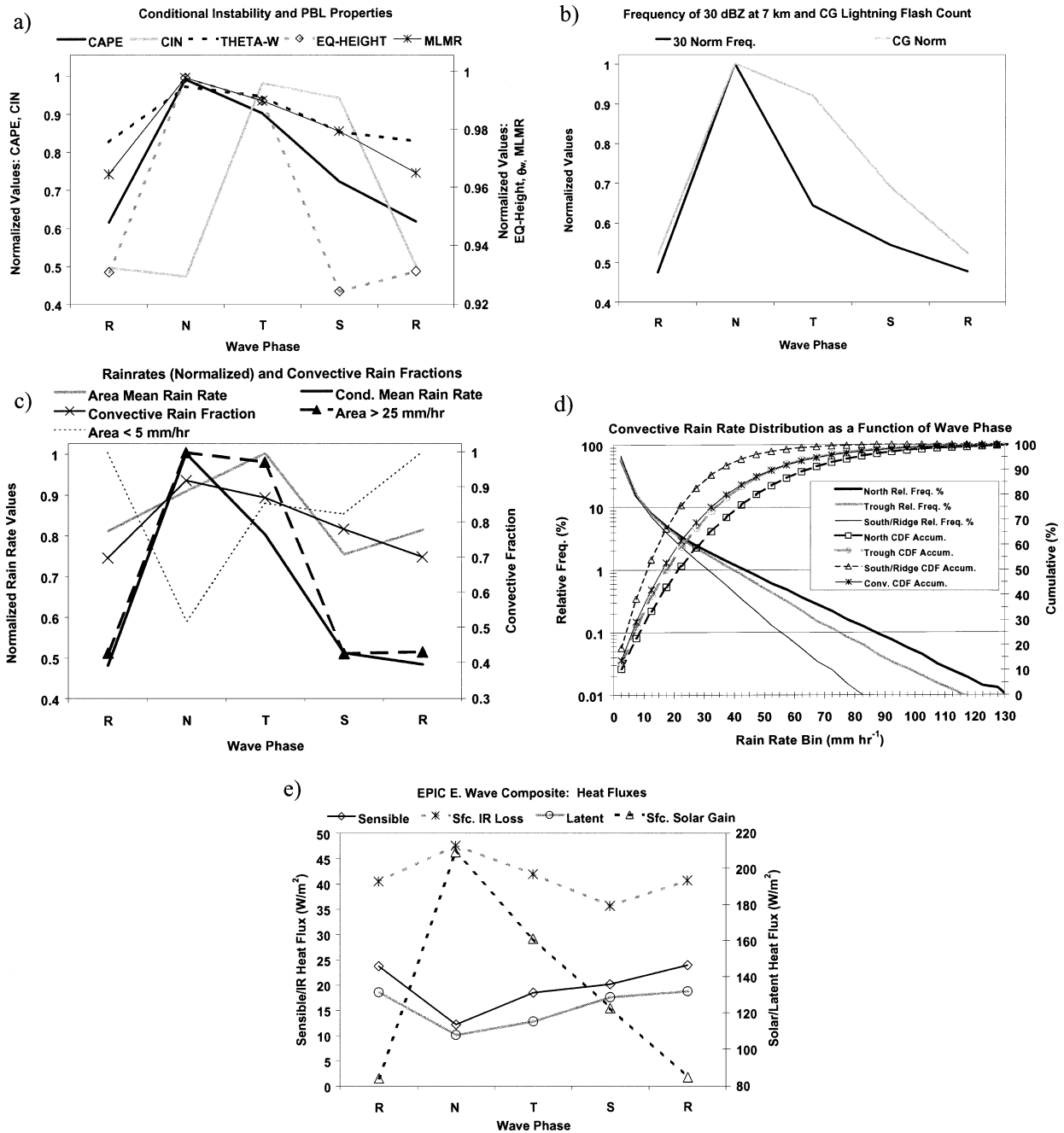
FIG. 14. Easterly wave composites for instability, rainfall, convective structure, and surface flux parameters in the ridge (R), northerly (N), trough (T), and southerly (S) phases. (a) Normalized values of CAPE, CIN, equilibrium-level height (EQ-HEIGHT), mixed-layer θ_w, and MLMR; (b) normalized frequency of reflectivity $\geq$30 dBZ at 7 km and, normalized CG lightning flash counts; (c) normalized area coverages of rain rates $\geq$25 mm h^{-1} and $\leq$5 mm h^{-1}, normalized area mean rain rate, normalized conditional mean rain rate (all on left ordinate), and values of convective rain fraction (right ordinate); (d) as in Fig. 8, but convective rainfall distributions partitioned by easterly wave phase; and (e) *RHB* mean values of sensible heat fluxes (left ordinate), latent heat fluxes (right ordinate), net surface solar and IR radiative fluxes (right ordinate). All fluxes expressed in units of W m^{-2}.

gence and attendant upper-level divergence above 8 km occurs as the wave phase transitions to the trough and southerly regimes, consistent with the presence of more midlevel cloudiness and stratiform precipitation (and perhaps some melting-induced convergence near the

4.5–5-km level). In turn, the vertical motion profiles exhibit upward motion above 5 km and weak downward motion below 5 km (similar to the archetypical meso-scale convective system stratiform region vertical mo-tion profile; e.g., Houze 1993). Interestingly, the ridge
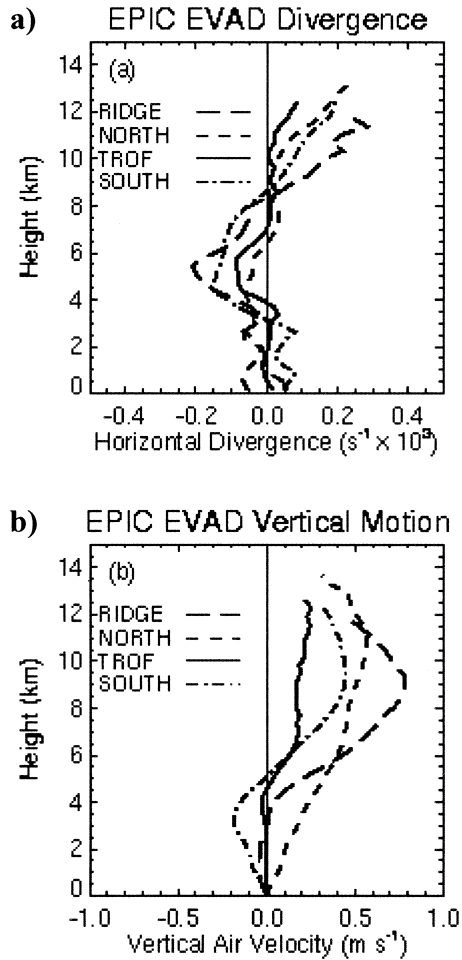
a) EPIC EVAD Divergence

b) EPIC EVAD Vertical Motion

FIG. 15. Composited EVAD analyses for each easterly wave phase of mean (a) divergence ($\times 10^{-3}$ s^{-1}) and (b) vertical motion (m s^{-1}).

phase divergence profile does not exhibit a midlevel divergence signature (in contrast to Thompson et al. 1979), which would be expected if the intermediate mode of a trimodal convective cloud-top distribution were dominant (Johnson et al. 1999). Instead, the ridge phase exhibits even more enhanced midlevel convergence (and attendant upper-level upward air motion; Fig. 15b) and upper-level divergence. In reality, it is likely that the ridge divergence and vertical motion profiles for the ridge phase are an artifact/bias of 1) the large stratiform event of 24 September (Fig. 7a); and 2) the EVAD technique, as this technique requires broad echo coverage, severely restricting the applicable convective system sample size. Smaller areas of isolated convection present during the ridge phase would not satisfy this constraint, and hence would not be incorporated into the average.

7. Summary and conclusions

During September 2001, three easterly wave passages were observed at the location of the R/V *Ronald H.*

Brown during the EPIC-2001 ITCZ field campaign over the eastern Pacific warm pool. In addition to tropospheric wind and thermodynamic analyses, we presented unique observations of the 4D precipitation structure associated with each wave passage using shipborne C-band Doppler radar data. Following earlier studies, we partitioned the thermodynamic, kinematic *and* precipitation structure observations into ¼-wavelength phases (ridge, northerly, trough, southerly) based on the *v*-wind direction and speed at 700 hPa. This was done in order to construct a "composite easterly wave" as a function of wave phase and height representative of the EPIC 2001 ITCZ observations.

The composite observations revealed positively correlated *u* and *v* winds possessing a westward phase tilt with height, consistent with the presence of deep-tropospheric northeasterly shear. Deep-tropospheric shear was at a maximum (minimum) during the southerly (northerly) phase. Concomitant temperature and humidity perturbations did not exhibit a pronounced phase tilt with height, but did exhibit mid- to upper-level cooling (warming) and drying (moistening), low-level warming (cooling) and moistening (drying), and associated increases (decreases) in CAPE during the northerly (trough and southerly) phase, similar to previous studies of African easterly waves. Enhanced latent and sensible heat fluxes lead the increased CAPE in the northerly phase, ramping up in the trough and southerly phases and reaching a maximum during the preceding ridge phase. Surface solar (IR) gain (loss) was also at a maximum during the northerly phase, providing further fuel for the generation of CAPE.

As suggested by the trends in instability, convective vertical structure, area coverage and rain rates were strongly modulated by the passage of each wave. Peaks in echo-top height, conditional mean rain rate, convective rain volume fraction (>90%), area coverage of heavy rain, and the *vertical* intensity of convection, as measured by the vertical extension of reflectivities ≥30 dBZ and cloud-to-ground lightning flash counts, all tended to occur 0–2 days prior to the passage of the wave trough during the northerly phase. Relatively high echo-top heights and more widespread light convective and stratiform precipitation, with a lower convective rain volume fraction (~70%–80%) persisted behind the trough in the southerly and ridge phases, however the vertical intensity of the convection and associated area coverage of heavy convective rain were diminished. This suggests that a transition in convective diabatic heating structure and precipitation process occurred across the wave; beginning with heavier raining, lightning-producing convection in the pretrough northerly phase (indicative of more prolific ice processes) and transitioning to weaker/decaying convection and stratiform rainfall in and behind the wave trough.

Importantly, the area-averaged rain rate in each phase differed by only 10%–15% from the mean (13 mm day^{-1}) across the wave. This is an important point be-

cause it suggests that the integrated latent heating in each phase was similar. If this is the case, then the systematic changes in rain-rate distribution and convective vertical structure observed as a function of easterly wave phase imply a similar systematic change in the vertical profile of diabatic heating across the wave (e.g., Tao et al. 1990, 1993). These changes should, in turn, feedback to the synoptic-scale dynamics of the easterly waves. Both the changes in diabatic heating profile and feedbacks to the synoptic scale could be examined in future cloud-resolving modeling studies, and the shipboard observations obtained in EPIC-2001, especially the radar observations, would serve as an important validation dataset for these modeling studies.

REFERENCES

Albignat, J. P., and R. J. Reed, 1980: The origin of African wave disturbances during phase III of GATE. *Mon. Wea. Rev.,* **108,** 1827–1839.

Austin, P. M., and R. A. Houze Jr., 1972: Analysis of the structure of precipitation patterns in New England. *J. Appl. Meteor.,* **11,** 926–935.

Avila, L. A., and R. J. Pasch, 1992: Atlantic tropical systems of 1991. *Mon. Wea. Rev.,* **120,** 2688–2696.

Berg, W., C. Kummerow, and C. A. Morales, 2002: Differences between east and west Pacific rainfall systems. *J. Climate,* **15,** 3659–3672.

Boccippio, D. J., S. J. Goodman, and S. Heckman, 2000: Regional differences in tropical lightning distributions. *J. Appl. Meteor.,* **39,** 2231–2248.

Burpee, R. W., 1972: The origin and structure of easterly waves in the lower troposphere of North Africa. *J. Atmos. Sci.,* **29,** 77–90.

——, 1974: Characteristics of North African easterly waves during the summers of 1968 and 1969. *J. Atmos. Sci.,* **31,** 1556–1570.

——, 1975: Some features of synoptic-scale waves based on a compositing analysis of GATE data. *Mon. Wea. Rev.,* **103,** 921–925.

Carey, L. D., and S. A. Rutledge, 2000: The relationship between precipitation and lightning in tropical island convection: A C-band polarimetric radar study. *Mon. Wea. Rev.,* **128,** 2687–2710.

Chang, C.-P., 1970: Westward propagating cloud patterns in the tropical Pacific as seen from time composite satellite photographs. *J. Atmos. Sci.,* **27,** 133–138.

——, V. F. Morris, and J. M. Wallace, 1970: A statistical study of easterly waves in the western Pacific: July–December 1964. *J. Atmos. Sci.,* **27,** 195–201.

Cheng, C., and R. A. Houze Jr., 1979: The distribution of convective and mesoscale precipitation in GATE radar echo patterns. *Mon. Wea. Rev.,* **107,** 1370–1381.

Cifelli, R., S. A. Rutledge, D. J. Boccippio, and T. Matejka, 1996: Horizontal divergence and vertical velocity retrievals from Doppler radar and wind profiler observations. *J. Atmos. Oceanic Technol.,* **13,** 948–966.

Cramer, J. A., and K. L. Cummins, 1999: Long-range and transoceanic lightning detection. Preprints, *11th Int. Conf. on Atmospheric Electricity,* Guntersville, AL, NASA, 250–253.

Cronin, M. F., N. Bond, C. Fairall, J. Hare, M. J. McPhaden, and R. A. Weller, 2002: Enhanced oceanic and atmospheric monitoring underway in the eastern Pacific. *Eos, Trans. Amer. Geophys. Union,* **83,** 205–211.

DeMott, C. A., and S. A. Rutledge, 1998a: The vertical structure of TOGA COARE convection. Part I: Radar echo distributions. *J. Atmos. Sci.,* **55,** 2730–2747.

——, and ——, 1998b: The vertical structure of TOGA COARE convection. Part II: Modulating influences and implications for diabatic heating. *J. Atmos. Sci.,* **55,** 2748–2762.

Donner, L. J., C. J. Seman, and R. S. Hemler, 1999: Three-dimensional cloud-system modeling of GATE convection. *J. Atmos. Sci.,* **56,** 1885–1912.

Duvel, J. P., 1990: Convection over tropical Africa and the Atlantic Ocean during northern summer. Part II: Modulation by easterly waves. *Mon. Wea. Rev.,* **118,** 1855–1868.

Dye, J. E., J. J. Jones, A. J. Weinheimer, and W. P. Winn, 1988: Observations within two regions of charge during initial thunderstorm electrification. *Quart. J. Roy. Meteor. Soc.,* **114,** 1271–1290.

Edson, J. B., A. A. Hinton, K. E. Prada, J. E. Hare, and C. W. Fairall, 1998: Direct covariance flux estimates from moving platforms at sea. *J. Atmos. Oceanic Technol.,* **15,** 547–562.

Fairall, C. W., E. F. Bradley, J. S. Godfrey, G. A. Wick, J. B. Edson, and G. S. Young, 1996a: Cool skin and warm layer effects on the sea surface temperature. *J. Geophys. Res.,* **101,** 1295–1308.

——, ——, D. P. Rogers, J. B. Edson, and G. S Young, 1996b: Bulk parameterization of air–sea fluxes in TOGA COARE. *J. Geophys. Res.,* **101,** 3747–3767.

——, ——, J. E. Hare, A. A. Grachev, and J. B. Edson, 2003: Bulk parameterization of air–sea fluxes: Updates and verification for the COARE algorithm. *J. Climate,* **16,** 571–591.

Goodman, S. J., D. E., Buechler, P. D. Wright, and W. D. Rust, 1988: Lightning and precipitation history of a microburst-producing storm. *Geophys. Res. Lett.,* **15,** 1185–1188.

Grabowski, W. W., X. Wu, and M. W. Moncrieff, 1996: Cloud-resolving modeling of tropical cloud systems during Phase II of GATE. Part I: Two-dimensional experiments. *J. Atmos. Sci.,* **53,** 3684–3709.

Gu, G., and C. Zhang, 2002: Westward-propagating synoptic-scale disturbances and the ITCZ. *J. Atmos. Sci.,* **59,** 1062–1075.

Holton, J. R., 1971: A diagnostic model for equatorial wave disturbances: The role of vertical shear of the mean zonal wind. *J. Atmos. Sci.,* **28,** 55–64.

Houze, R. A., Jr., 1993: *Cloud Dynamics.* Academic Press, 573 pp.

Hudlow, M. D., 1979: Mean rainfall patterns for the three phases of GATE. *J. Appl. Meteor.,* **18,** 1656–1669.

Jenkins, M. A., and H.-R. Cho, 1991: An observational study of the first-order vorticity dynamics in a tropical easterly wave. *J. Atmos. Sci.,* **48,** 965–975.

Johnson, R. H., T. M. Rickenbach, S. A. Rutledge, P. E. Ciesielski, and W. H. Schubert, 1999: Trimodal characteristics of tropical convection. *J. Climate,* **12,** 2397–2418.

Kwon, H. J., and M. Mak, 1990: A study of the structural transformation of the African easterly waves. *J. Atmos. Sci.,* **47,** 277–292.

Landsea, C. W., G. D. Bell, W. M. Gray, and S. B. Goldenberg, 1998: The extremely active 1995 Atlantic hurricane season: Environmental conditions and verification of seasonal forecasts. *Mon. Wea. Rev.,* **126,** 1174–1193.

Lau, K.-H., and N.-C. Lau, 1990: Observed structure and propagation characteristics of tropical summertime synoptic scale disturbances. *Mon. Wea. Rev.,* **118,** 1888–1913.

Liebman, B., and H. H. Hendon, 1990: Synoptic-scale disturbances near the equator. *J. Atmos. Sci.,* **47,** 1463–1479.

Loehrer, S. M., T. A. Edmands, and J. A. Moore, 1996: TOGA COARE upper-air sounding data archive: Development and quality control procedures. *Bull. Amer. Meteor. Soc.,* **77,** 2651–2672.

Matejka, T., and R. C. Srivastava, 1991: An improved version of the extended velocity–azimuth display analysis of single-Doppler radar data. *J. Atmos. Oceanic Technol.,* **8,** 453–466.

Mohr, C. G., 1986: Merger of mesoscale datasets into a common Cartesian format for efficient and systematic analyses. *J. Atmos. Oceanic Technol.,* **3,** 143–161.

Molinari, J., D. Knight, M. Dickinson, D. Vollaro, and S. Skubis, 1997: Potential vorticity, easterly waves, and tropical cyclogenesis. *Mon. Wea. Rev.,* **125,** 2699–2708.

——, D. Vollaro, S. Skubis, and M. Dickinson, 2000: Origins and mechanisms of eastern Pacific tropical cyclogenesis: A case study. *Mon. Wea. Rev.,* **128,** 125–139.

Nesbitt, S. W., E. J. Zipser, and D. J. Cecil, 2000: A census of precipitation features in the Tropics using TRMM: Radar, ice scattering, and lightning observations. *J. Climate,* **13,** 4087–4106.

Nitta, T., 1977: Response of cumulus updraft and downdraft to GATE A/B-scale motion systems. *J. Atmos. Sci.,* **34,** 1163–1186.

Norquist, D. C., E. E. Recker, and R. J. Reed, 1977: The energetics of African wave disturbances as observed during phase III of GATE. *Mon. Wea. Rev.,* **105,** 334–342.

Petersen, W. A., and S. A. Rutledge, 2001: Regional variability in tropical convection: Observations from TRMM. *J. Climate,* **14,** 3566–3586.

——, ——, and R. E. Orville, 1996: Cloud-to-ground lightning observations from TOGA COARE: Selected results and lightning location algorithms. *Mon. Wea. Rev.,* **124,** 602–620.

——, S. W. Nesbitt, R. J. Blakeslee, R. Cifelli, P. Hein, and S. A. Rutledge, 2002: TRMM observations of intraseasonal variability in convective regimes over the Amazon. *J. Climate,* **15,** 1278–1294.

Raymond, D. J., C. Lopez-Carillo, and L. L. Cavazos, 1998: Case-studies of developing east Pacific easterly waves. *Quart. J. Roy. Meteor. Soc.,* **124,** 2005–2034.

——, G. Raga, C. Bretherton, J. Molinari, C. Lopez-Carrillo, and Z. Fuchs, 2003: Convective forcing in the intertropical convergence zone of the eastern Pacific. *J. Atmos. Sci.,* in press.

Reed, R. J., and E. E. Recker, 1971: Structure and properties of synoptic-scale wave disturbances in the equatorial western Pacific. *J. Atmos. Sci.,* **28,** 1117–1133.

——, D. C. Norquist, and E. E. Recker, 1977: The structure and properties of African wave disturbances as observed during Phase III of GATE. *Mon. Wea. Rev.,* **105,** 317–333.

——, A. Hollingsworth, W. A. Heckley, and F. Delsol, 1988: An evaluation of the performance of the ECMWF operation system in analyzing and forecasting easterly wave disturbances over Africa and the tropical Atlantic. *Mon. Wea. Rev.,* **116,** 824–865.

Reeves, R. W., C. F. Ropelewski, and M. D. Hudlow, 1979: Relationships between large-scale motion and convective precipitation during GATE. *Mon. Wea. Rev.,* **107,** 1154–1168.

Rickenbach, T. M., and S. A. Rutledge, 1998: Convection in TOGA COARE: Horizontal scale, morphology, and rainfall production. *J. Atmos. Sci.,* **55,** 2715–2729.

Riehl, H., 1954: *Tropical Meteorology.* McGraw Hill, 392 pp.

Rutledge, S. A., E. R. Williams, and T. D. Keenan, 1992: The Down Under Doppler and Electricity Experiment (DUNDEE): Overview and preliminary results. *Bull. Amer. Meteor. Soc.,* **73,** 3–16.

Ryan, M., M. J. Post, B. Martner, J. Novak, and L. Davis, 2002: The NOAA *Ron Brown's* shipboard Doppler precipitation radar. Pre-

prints, *Sixth Symp. on Integrated Observing Systems,* Orlando, FL, Amer. Meteor. Soc., 46–48.

Saxen, T. R., and S. A. Rutledge, 1998: Surface fluxes and boundary layer recovery in TOGA COARE: Sensitivity to convective organization. *J. Atmos. Sci.,* **55,** 2763–2781.

Serra, Y. L., and R. A. Houze Jr., 2002: Observations of variability on synoptic timescales in the east Pacific ITCZ. *J. Atmos. Sci.,* **59,** 1723–1743.

Shapiro, L. J., 1986: The three-dimensional structure of synoptic-scale disturbances over the tropical Atlantic. *Mon. Wea. Rev.,* **114,** 1876–1891.

Srivastava, R. C., T. J. Matejka, and T. J. Lorello, 1986: Doppler radar study of the trailing anvil region associated with a squall line. *J. Atmos. Sci.,* **43,** 356–377.

Steiner, M., R. A. Houze Jr., and S. E. Yuter, 1995: Climatological characterization of three-dimensional storm structure from operational radar and rain gauge data. *J. Appl. Meteor.,* **34,** 1978–2007.

Stevens, D. E., 1979: Vorticity, momentum and divergence budgets of synoptic-scale wave disturbances in the tropical eastern Atlantic. *Mon. Wea. Rev.,* **107,** 535–550.

Tao, W.-K., J. Simpson, S. Lang, M. McCumber, R. Adler, and R. Penc, 1990: An algorithm to estimate the heating budget from vertical hydrometeor profiles. *J. Appl. Meteor.,* **29,** 1232–1244.

——, S. Lang, J. Simpson, and R. Adler, 1993: Further development and testing of the heating retrieval algorithm for TRMM. *J. Meteor. Soc. Japan,* **71,** 685–700.

Thompson, R. M., Jr., S. W. Payne, E. E. Recker, and R. J. Reed, 1979: Structure and properties of synoptic-scale wave disturbances in the intertropical convergence zone of the eastern Atlantic. *J. Atmos. Sci.,* **36,** 53–72.

Thorncroft, C., and K. Hodges, 2001: African easterly wave variability and its relationship to Atlantic tropical cyclone activity. *J. Climate,* **14,** 1166–1179.

Tokay, A., and D. A. Short, 1996: Evidence from tropical raindrop spectra of the origin of rain from stratiform versus convective clouds. *J. Appl. Meteor.,* **35,** 355–371.

Toracinta, E. R., D. J. Cecil, E. J. Zipser, and S. W. Nesbitt, 2002: Radar, passive microwave, and lightning characteristics of precipitating systems in the Tropics. *Mon. Wea. Rev.,* **130,** 802–824.

Williams, E. R., S. A. Rutledge, S. C. Geotis, N. Renno, E. Rasmussen, and T. Rickenbach, 1992: A radar and electrical study of tropical hot towers. *J. Atmos. Sci.,* **49,** 1386–1395.

Xu, K.-M., and D. A. Randall, 2001: Explicit simulation of cumulus ensembles with the GATE phase III data: Budgets of a composite easterly wave. *Quart. J. Roy. Meteor. Soc.,* **127,** 1–21.

Yanai, M., and T. Nitta, 1967: Computation of vertical motion and vorticity budget in a Caribbean easterly wave. *J. Meteor. Soc. Japan,* **45,** 444–465.

——, T. Maruyama, T. Nitta, and Y. Hayashi, 1968: Power spectra of large-scale disturbances over the tropical Pacific. *J. Meteor. Soc. Japan,* **46,** 308–323.

Yuter, S. E., and R. A. Houze Jr., 2000: The 1997 Pan American Climate Studies Tropical Eastern Pacific Process Study. Part I: ITCZ region. *Bull. Amer. Meteor. Soc.,* **81,** 451–481.

Zehnder, J. A., D. M. Powell, and D. L. Ropp, 1999: The interaction of easterly waves, orography, and the intertropical convergence zone in the genesis of eastern Pacific tropical cyclones. *Mon. Wea. Rev.,* **127,** 1566–1585.

Zipser, E. J., and K. R. Lutz, 1994: The vertical profile of radar reflectivity of convective cells: A strong indicator of storm intensity and lightning probability? *Mon. Wea. Rev.,* **122,** 1751–1759.